UNIVERSIDADE TÉCNICA DO ATLÂNTICO

INSTITUTO DE ENGENHARIA E CIÊNCIAS DO MAR

WEST AFRICAN SCIENCE SERVICE CENTRE ON CLIMATE CHANGE AND ADAPTED LAND USE

Master Thesis

SIMULATIONS AND PROJECTIONS OF THE SOUTH ATLANTIC OCEAN DIPOLE IMPACTS ON REGIONAL RAINFALL IN CMIP6 MODELS

UZOMA C. NWORGU

Master Research Program on Climate Change and Marine Sciences

São Vicente
2023

UNIVERSIDADE TÉCNICA DO ATLÂNTICO
INSTITUTO DE ENGENHARIA E CIÊNCIAS DO MAR
WEST AFRICAN SCIENCE SERVICE CENTRE ON CLIMATE CHANGE AND ADAPTED LAND USE

Master Thesis

SIMULATIONS AND PROJECTIONS OF THE SOUTH ATLANTIC OCEAN DIPOLE IMPACTS ON REGIONAL RAINFALL IN CMIP6 MODELS

UZOMA C. NWORGU

Master Research Program on Climate Change and Marine Sciences

Supervisor | Prof. Hyacinth C. Nnamchi
Co-supervisor | Prof. Nilton Évora do Rosário

São Vicente
2023

UNIVERSIDADE TÉCNICA DO ATLÂNTICO

INSTITUTO DE ENGENHARIA E CIÊNCIAS DO MAR

WEST AFRICAN SCIENCE SERVICE CENTRE ON CLIMATE CHANGE AND ADAPTED LAND USE

Simulations and projections of the South Atlantic Ocean Dipole impacts on Regional Rainfall in CMIP6 Models

Uzoma C. Nworgu

Master's thesis presented to obtain the master's degree in Climate Change and Marine Sciences, by the Institute of Engineering and Marine Sciences, Atlantic Technical University in the framework of the West African Science Service Centre on Climate Change and Adapted Land Use

Supervisor

_____

Prof. Hyacinth C. Nnamchi
GEOMAR Helmholtz Centre for Ocean Research Kiel, Kiel, Germany

Co-supervisor

_____

Prof. Nilton Évora do Rosário
Federal University of São Paulo,SP, Brazil

São Vicente
2023

UNIVERSIDADE TÉCNICA DO ATLÂNTICO

INSTITUTO DE ENGENHARIA E CIÊNCIAS DO MAR

WEST AFRICAN SCIENCE SERVICE CENTRE ON CLIMATE CHANGE AND ADAPTED LAND USE

Simulations and projections of the South Atlantic Ocean Dipole impacts on Regional Rainfall in CMIP6 Models

Uzoma C. Nworgu

Panel defense

President

_____

Examiner 1

_____

Examiner 2

_____

São Vicente
2023

Publications list

Nworgu, U. C., Nnamchi, H.C. & Évora do Rosário, N. (2023). Projected Weakening of South Atlantic Impact On Regional Rainfall in CMIP6 Models. Manuscript under preparation for *Environmental Research: Climate.*

Nworgu, U. C. & Nnamchi, H.C, (2023, July 31-August 11). Simulations and Projections of the South Atlantic Ocean Dipole Impacts On Regional Rainfall in CMIP6 Models [Poster presentation]. Presented at the 4th ICTP Summer School on Theory, Mechanisms and Hierarchical Modeling of Climate Dynamics: Atlantic Variability and Tropical Basin Interactions at Interannual to Multi-Decadal Time Scales, Trieste, Italy.

Nworgu, U. C. (2023, June 5-June 16). Evaluating the South Atlantic Ocean Dipole Impacts on West African Precipitation in CMIP6 Model Simulations [Poster presentation/Talk]. Presented at the 2023 SOLAS Summer School, Cape Verde.

Olopade, O. A., Dienye, H. E., & Nworgu, U. C. (2020). Estimation of growth, mortality, and exploitation status of Nurse Tetra (*Brycinus nurse*) and True Big Scale Tetra (*Brycinus macrolepidotus*) (family: Alestidae) from the New Calabar River, Nigeria. *Indonesian Fisheries Research Journal*, *25*(2), 113. https://doi.org/10.15578/ifrj.25.2.2019.113-122

Financial support

The German Federal Ministry of Education and Research (BMBF) in the framework of the West African Science Service Centre on Climate Change and Adapted Land Use (WASCAL) through WASCAL Graduate Studies Programme in Climate Change and Marine Sciences at the Institute for Engineering and Marine Sciences, Atlantic Technical University, Cabo Verde.

Dedication

To,

Bobby, Kris, Mamah, and Ceasar with whom I’ve navigated the maze of early adulthood...

To Da5+,

GS, Joel, Jeffery, Sammy and Vincent with whom this dream began.

Acknowledgements

My deepest gratitude is given to The Almighty Father for His enduring love and mercies which have brought me this far in my life.

I want to express my deepest appreciation to my supervisor, Prof. Hyacinth C. Nnamchi for motivating and guiding me throughout this master thesis process. I could not have asked for a better supervisor and mentor. I owe a debt of gratitude to my co-supervisor, Prof. Nilton Évora do Rosário who was instrumental in stimulating my interest in this field of study.

I am equally thankful to the Director of WASCAL Cabo Verde, Dr. Corrine Almeida, the Deputy Director, Dr. António Pinto Almeida, and to the Scientific coordinator Dr. Estanislau Baptista Lima, for their support, encouragement and guidance which have punctuated my wonderful experience in Cabo Verde as a Master student.

To my parents Mr. Nick Nworgu and Mrs Joyce Nworgu, and my sisters Amaka and Izuchi; thank you for your prayers, support and continuous encouragement. It has truly kept me going.

To my friend, partner, confidant and everything inbetween; Miede, thank you for being through it all with me.

I would like to acknowledge the German Federal Ministry of Education and Research (BMBF) that fund the West Africa Science Service Center on Climate Change and Adapted Land Use (WASCAL) Master Program in Climate change and Marine Sciences.

I also express my heartfelt gratitude to all the staff of WASCAL Cabo Verde and the Institute of Engineering and Marine Sciences (ISECMAR) of the Atlantic Technical University (UTA) and also to all my lecturers for all forms of help and guidance they offered during my study period.

To my colleagues, the third batch of WASCAL Master program in Climate change and Marine sciences Cabo Verde, it has been my utmost pleasure to share this time in Cabo Verde with you. The sky is our starting point from here on. Cheers!

Resumo

Este estudo investiga os impactos do Dipolo do Oceano Atlântico Sul (SAOD) na precipitação sobre as áreas continentais adjacentes à região do Atlântico Sul durante o inverno austral (junho-julho-agosto), utilizando a última fase 6 do Projeto de Intercomparação de Modelos Acoplados (CMIP6). Consideramos um período de referência histórico (1950-2014) e alterações futuras no âmbito da Via Socioeconómica Partilhada 5-8.5 (SSP585) de 2015 a 2079. As análises históricas das observações revelaram quatro regiões com correlações espacialmente coerentes da precipitação com o SAOD, nomeadamente: Norte da Amazónia, Costa da Guiné, África Central e Sudeste do Brasil - um resultado no geral consistente com análises semelhantes presentes na literatura anterior. A média do conjunto de 44 simulações históricas dos modelos CMIP6 subestimou largamente a correlação entre o SAOD e chuva nestas regiões, enquanto o desempenho individual dos modelos revelou uma dispersão no comportamento em cada região. O desempenho dos modelos foi melhor na África Central, com 52% dos modelos a simularem uma correlação positiva estatisticamente significativa, semelhante às observações. O pior desempenho foi registrado no Sudeste do Brasil, com apenas 7% dos modelos a terem um bom desempenho, enquanto mais de 40% dos modelos simularam uma correlação de sinal contrário em relação às observações. As observações mostraram que a influência da SAOD na precipitação variou entre as regiões, sendo mais forte sobre a Costa da Guiné e mais fraca sobre o Sudeste do Brasil. As simulações futuras de um conjunto dos modelos com melhor desempenho em cada região indicaram uma diminuição da influência da SAOD na variabilidade da precipitação, em todas as regiões respectivas, no cenário SSP585. Os nossos resultados sublinham os impactos significativos do SAOD na variabilidade regional da precipitação e salientam a necessidade de melhorar a capacidade dos modelos CMIP6 para simular a relação SAOD-precipitação. Além disso, um futuro com emissões ininterruptas de gases com efeito de estufa poderá causar alterações significativas nos padrões de precipitação, conduzindo a impactos imprevisíveis nas regiões afectadas. Globalmente, estes resultados poderão constituir um primeiro passo útil para melhorar a previsão da variabilidade climática regional e planear a adaptação dos ecossistemas regionais e das actividades socioeconómicas humanas às alterações climáticas.

Palavra-chave: SAOD, Atlântico Sul, variabilidade da precipitação, modelos CMIP6

Abstract

This study investigates the impacts of the South Atlantic Ocean Dipole (SAOD) on rainfall over land areas of the South Atlantic region during austral winter (June-July-August), using the latest Coupled Model Intercomparison Project phase 6 (CMIP6). We consider a historical reference period (1950-2014) and, future changes under the Shared Socioeconomic Pathway 5-8.5 (SSP585) from 2015 to 2079. Our historical analyses of observations revealed four regions with spatially-coherent correlations of grid-point rainfall with the SAOD namely; Northern Amazon, Guinea Coast, Central Africa and South East Brazil – a result generally consistent with similar analyses in earlier literature. The ensemble mean of 44 CMIP6 models' historical simulations largely underestimated the SAOD-rainfall correlation in these regions, while individual model performance revealed a spread in model behavior in each region. Model performance was best in Central Africa with 52% of the models simulating statistically significant positive correlations, similar to observations. The worst performance was for South East Brazil with only 7% of the models performing well, while over the Guinea Coast and South East Brazil, more than 40% of the models simulated a negative sign correlation in opposition to observations. Observations showed that SAOD influence on rainfall varied between the regions, being strongest over the Guinea Coast and weakest over South East Brazil. Future simulations of an ensemble of the best-performing models in each region indicated a decrease in SAOD influence on rainfall variability, in all the respective regions, under the SSP585 scenario. Our results underscore the significant impacts of SAOD on regional rainfall variability and highlights the need to enhance CMIP6 models' ability to simulate the SAOD-rainfall relationship. Furthermore, a future with unabated greenhouse gas emissions could cause significant changes in rainfall patterns, leading to unpredictable impacts on the affected regions. Overall, these results could be a useful first step in improving the prediction of regional climate variability and planning adaptation of the regional ecosystems and human socio-economic activities to climate change.

Keyword: SAOD, South Atlantic, Rainfall variability, CMIP6 models

Abbreviations and acronyms

CA	Central Africa
Cat1EnsMean	Ensemble Mean of Category 1 (best performing) models
CMIP6	Coupled Model Intercomparison Project Phase 6
DJF	December-January-February
ENSO	El Niño-Southern Oscillation
EOF	Empirical Orthogonal Function
GCM	Global Climate Model
GHG	Green House Gas
GPCC	Global Precipitation Climatology Centre
HadISST	Hadley Centre Global Sea Ice and Sea Surface Temperature
ITCZ	InterTropical Convergence Zone
JJA	June-July-August
MAM	March-April-May
MMM	Multi-Model Mean
NCAR	National Center for Atmospheric Research
NCL	NCAR Command Language
NEP	North East Pole
Obs	Observations
SACZ	South American Convergence Zone
SAD	South Atlantic Dipole
SAO	South Atlantic Ocean

SAOD	South Atlantic Ocean Dipole
SAODI	South Atlantic Ocean Dipole Index
SASD	South Atlantic Subtropical Dipole
SEB	South East Brazil
SLP	Sea Level Pressure
SPEEDY	Simplified Parameterizations, primitivE-Equation Dynamics
SSP585	Shared Socioeconomic Pathway 5 – 8.5
SST	Sea Surface Temperature
SSTA	Sea Surface Temperature Anomaly
SWP	South Western Pole
UCLA-AGCM	University of California, Los Angeles Atmospheric General Circulation Model.
WAM	West African Monsoon

List Of Contents

Publications list....i
Financial support....ii
Dedication....iii
Acknowledgements....iv
Resumo....v
Abstract....vi
Abbreviations and acronyms....vii
Figure index....xi
Tables index....xiii
1. Introduction....1
1.1 Objectives of the Study....3
2. Literature Review....5
2.1 Modes of Variability in the South Atlantic....5
2.2 SAOD versus SASD....6
2.3 Impacts of South Atlantic variability on Regional Climate....8
2.4 Modeling of the South Atlantic modes of variability and their impacts....8
3. Materials and Methods....10
3.1 Study Region....10
3.2 Data collection and description....13
3.3 Data analyses....18
4. Results....23
4.1 Evaluation of the SAOD-rainfall relationship in CMIP6 historical ensemble 1950-2014 23
4.1.1 SAOD Timeseries from Observations and CMIP6 historical ensemble....23
4.1.2 Relationship between the SAOD and Rainfall map in Observations and CMIP6 historical ensemble....26
4.1.3 Relationship between the SAODI and rainfall indices in the CMIP6 historical ensemble....30
4.2 Projections of the SAOD-Rainfall relationship in CMIP6 SSP585 ensemble (2015-2079)....36
4.2.1 Spatial pattern of the projected SAOD-rainfall relationship....36
4.2.2 Projections of SAOD impact on the regionally-averaged rainfall....38
4.2.3 A weakening of the SAOD impacts on regional rainfall under SSP585....42
5. Discussion....45

6. Conclusion.....49
7. Recommendations.....50
8. References.....51
Appendix.....61
Data availability.....66

Figure index

Figure 1: Sea surface temperature (RED, warming; BLUE, cooling), mean sea level pressure (contours) and surface wind anomalies (vectors) associated with the SAOD (from (Nnamchi et al., 2011).....7

Figure 2: Map of study area indicating the four (4) regions in the South Atlantic considered (black boxes). [CA = Central Africa, SE_Brazil = South East Brazil]. Oceanic region of the South Atlantic is enclosed in dashed box.....13

Figure 3: Geographical location of the North East Pole (black solid box) [NEP; 10°E–20°W, 0°–15°S] and South West Pole (blue dashed box) [SWP; 10°– 40°W, 25°– 40°S] used to calculate the SAOD index.....19

Figure 4: Normalized SAODI time series for JJA from observations (HadISST) data (a) and CMIP6 ensemble mean (b). Red troughs indicate positive phase of SAOD while blue troughs indicate negative phase of SAOD. Standard deviations in (°C).....24

Figure 5: Normalized SAODI timeseries from CMIP6 model ensemble for the JJA season.. 25

Figure 6: Spatial correlation (historical) of SAODI and rainfall anomalies (from observations data) in land regions adjacent to the South Atlantic. White contours represent areas with significant correlation ($p < 0.05$). Black boxes delineate regions of statistically significant correlation; 1 – Amazon, 2 – Guinea Coast, 3 – Central Africa, 4 – South East Brazil (SE_Brazil).....27

Figure 7: Spatial correlation of (historical) of SAODI and rainfall anomalies for individual CMIP6 models.....28

Figure 8: Correlation of SAODI and rainfall anomalies in JJA from observations (a) and multi-model mean (b). White contours indicate areas of statistically significant correlation while black boxes delineate the domains. 1 – Northern Amazon, 2 – Guinea Coast, 3 – Central Africa, 4 – South East Brazil (SE_Brazil).....29

Figure 9: Scatterplot of correlation values (x – axis) against the significance level [p – value] (y – axis) of individual model simulation of SAODI-rainfall correlation in Northern Amazon region. Observation = Red circle, Multi-Model Mean; (mmm = green circle, mmm2 = blue circle). Horizontal dotted line is where $p = 0.05$. Data points at or below the horizontal line are statistically significant at 95% confidence level ($p \leq 0.05$).....31

Figure 10: Scatterplot of correlation values (x – axis) against the significance level [p – value] (y – axis) of individual model simulation of SAODI-rainfall correlation in Guinea Coast region. Observation = Red circle, Multi-Model Mean; (mmm = green circle, mmm2 = blue circle). Horizontal dotted line is where $p = 0.05$. Data points at or below the horizontal line are statistically significant at 95% confidence level ($p \leq 0.05$).....32

Figure 11: Scatterplot of correlation values (x – axis) against the significance level [p – value] (y – axis) of individual model simulation of SAODI-rainfall correlation in Central Africa region. Observation = Red circle, Multi-Model Mean; (mmm = green circle, mmm2 = blue circle). Horizontal dotted line is where $p = 0.05$. Data points at or below the horizontal line are statistically significant at 95% confidence level ($p \leq 0.05$).....34

Figure 12: Scatterplot of correlation values (x – axis) against the significance level [p – value] (y – axis) of individual model simulation of SAODI-rainfall correlation in South East Brazil region. Observation = Red circle, Multi-Model Mean; (mmm = green circle, mmm2 =

blue circle). Horizontal dotted line is where p = 0.05. Data points at or below the horizontal line are statistically significant at 95% confidence level ($p \leq 0.05$).....35

Figure 13: Regression of rainfall anomalies on SAODI from CMIP6 models for JJA in historical (top [a]) and SSP585 projection (middle [b]). Map of the difference between [a] and [b] is shown in [c]. Dashed boxes delineate the domains: 1 – Amazon, 2 – Guinea Coast, 3 – Central Africa, 4 – South East Brazil (SE_Brazil).....37

Figure 14: Regression of rainfall anomalies on normalized SAOD for Northern Amazon showing historical (blue bars) and projected (red bars) simulations. Observations is represented as the dotted horizontal line. Obs stde = Standard error of observations. The black error bars indicate the model standard error.....39

Figure 15: Regression of rainfall anomalies on normalized SAOD for Guinea Coast showing historical (blue bars) and projected (red bars) simulations. Observations is represented as the dotted horizontal line. Obs stde = Standard error of observations. The black error bars indicate the model standard error.....39

Figure 16: Regression of rainfall anomalies on normalized SAOD for Central Africa showing historical (blue bars) and projected (red bars) simulations. Observations is represented as the dotted horizontal line. Obs stde = Standard error of observations. The black error bars indicate the model standard error.....41

Figure 17: Regression of rainfall anomalies on normalized SAOD for South East Brazil showing historical (blue bars) and projected (red bars) simulations. Observations is represented as the dotted horizontal line. Obs stde = Standard error of observations. The black error bars indicate the model standard error.....42

Figure 18: Ensemble mean of Category 1 models in each region. Blue error bars on Observations indicate the standard error for Observations at 95% confidence level. Historical and SSP585 bars that overlap with the error bars are not significantly different from Observations, while bars that fall beyond the error bars are significantly different from Observations.....44

Tables index

Table 1: Information of the 44 CMIP6 models used to construct the analyzed ensemble.....15

1. Introduction

The South Atlantic region encompasses a vast area of the Atlantic Ocean located between the equator and the southern tip of Africa and South America [45°S (latitude)]. It is characterized by a unique geographic location and oceanic features. The South Atlantic is bounded by South America to the west, Africa to the east, Antarctica to the south, and the North Atlantic to the north. The basic state of the ocean and climate in this region are determined by several factors. These include ocean currents and atmospheric circulation on local, regional, and global scales, as well as interactions with the adjacent continental landmasses. The sea surface temperatures (SST) in the South Atlantic region generally range from around 20°C in the north to 10°C or lower in the south, with the warmest waters typically found near the equator and along the eastern coast of South America[1].

The mean atmospheric circulation is dominated by the St. Helena subtropical anticyclone: a high-pressure system centered around 30°S over the South Atlantic[1]. This anticyclone is a quasi-permanent high-pressure system that derives its name from its location near the island of St. Helena in the southeastern South Atlantic. It is characterized by an anti-clockwise rotation of winds around the high-pressure center. These winds can be linked to the southeast trade winds close to the equator, whereas a band of dominant westerlies stretches south of about 40°S over the Southern Ocean. The St. Helena high-pressure system is therefore divided into northern and southern sections by the trade winds and westerly wind belts, respectively. Associated with the westerlies is a maximum in South Atlantic's wind convergence (or Ekman forcing) in the area around 40°S. These patterns exhibit considerable seasonality (Muller-Karger, et al., 2017). The large-scale winds set up the South Atlantic Ocean gyre, the southern boundary of this gyre being the Antarctic Circumpolar Current, the world’s largest ocean current.

The South Atlantic hosts several major Ocean currents. The South Equatorial Current moves in a westerly direction in proximity to the equator. Simultaneously, the Brazil Current carries warm waters towards the southern regions of the eastern South American coastline. Conversely, the Benguela Current travels northward along the southwestern shores of Africa, delivering cold waters, abundant in nutrients to the surface. Another important current in the region is the Malvinas Current (also known as the Falkland Current) which flows northward along the eastern shoreline of Argentina. It brings cold and nutrient-rich waters from the

1 See Appendix, Figures A1 - A3

Southern Ocean, contributing to the region's high biological productivity and supporting the rich marine ecosystems.

Superimposed on the atmospheric and oceanic circulations, rainfall in this region is largely determined by the Intertropical Convergence Zone (ITCZ) (Nnamchi et al., 2021; Schlosser et al., 2014) and the South Atlantic Convergence Zone (SACZ) (Pezzi et al., 2022). These zones are characterized by the convergence of trade winds that often result in large-scale rainfall. Overall, the South Atlantic region goes through marked seasonal changes, with summer taking place between December and February, and winter spanning from June to August. The peak rainfall associated with the ITCZ occurs in austral winter and that associated with SACZ is strongest in austral summer.

The leading mode of the ocean-atmosphere coupled variability over the South Atlantic is the South Atlantic Ocean dipole (SAOD), also referred to as the South Atlantic subtropical dipole (SASD) (Morioka et al., 2011; Nnamchi et al., 2017; Sterl & Hazeleger, 2003; Trzaska et al., 2007; Venegas et al., 1996, 1997), South Atlantic SST dipole (Haarsma et al., 2003) or simply South Atlantic dipole (Bombardi et al., 2014a). These definitions of the mode are strongly related (Nnamchi et al., 2017), and here we adopt the term SAOD.

The SAOD peaks in the austral winter (that is June-July-August, JJA) and is characterized by contrasting SST anomalies between the northeastern and southwestern parts of the South Atlantic. The positive (negative) phase occurs when the northeast South Atlantic is anomalously warm (cold) and the southwest is anomalously cold (warm). The SAOD originates from oscillation in the strength of the St. Helena anticyclone (Venegas et al., 1996; 1997), which drives changes in the net heat flux (Santis et al., 2020; Sterl & Hazeleger, 2003; Trzaska et al., 2007) and changes in the mixed layer depth (Sterl and Hazeleger, 2003; Santis et al., 2020). The SAOD is strongly related to the Atlantic Niño, the dominant mode of interannual variability over the tropical Atlantic (Foltz et al., 2019; Keenlyside & Latif, 2007; Zebiak, 1993) through the interaction of the St. Helena anticyclone and the southeasterly trade winds (Nnamchi et al., 2016). The SAOD is also related to the Benguela Niño off the coast of Angola, which itself is closely linked to the Atlantic Niño dynamics (Imbol Koungue et al., 2021; Lübbecke et al., 2010; Richter et al., 2010).

The SAOD exerts significant influences on climate variability over the adjacent continental land areas of Africa and South America. The characteristic SST patterns are associated with shifts in atmospheric circulation that modulate regional rainfall patterns. Specifically, the

SAOD drives increased convergence in the Atlantic ITCZ region leading to increased rainfall over the Guinea Coast and Central Africa and decreased rainfall in the SACZ/South East Brazil (Nnamchi et al., 2013; Wainer et al., 2021).

Large populations in regions such as West Africa, Central Africa, Southern Africa and South America all rely on rain-fed agriculture (Sultan & Gaetani, 2016; Wani et al., 2009). The livelihoods of rural communities that depend on agriculture and livestock farming are greatly impacted by rainfall as some of these regions lack adequate irrigation infrastructure (Boko et al., 2007). The industrial regions are also impacted by rainfall as it replenishes the water sources used for Hydropower generation (Conway et al., 2017). Rainfall also influences the health and productivity of ecosystems, supporting biodiversity and ecosystem services, most notably the tropical rainforests of the Amazon, Guinea Coast, and Central Africa (Bonal et al., 2016). Rainfall variability, including events such as droughts, floods, or shifts in seasonal patterns, can have profound socio-economic implications. These include impacts on food production, water resources, energy generation, rural livelihoods, and ecosystem services. Understanding and adapting to rainfall variability and change under increasing greenhouse forcing are, therefore, critical for sustainable development and building resilience in these socio-economic sectors.

The use of climate models can help us better understand how regional rainfall will change in the future in relation to the SAOD. The Coupled Model Intercomparison Project phase 6 (CMIP6; Eyring et al., 2016) is the latest internationally coordinated ensemble of state-of-the-art global climate models. However, it remains unclear how well the CMIP6 models represent the SAOD-regional rainfall variability, and how this relationship will change under future greenhouse emissions. This is an important first step in planning adaptation of the regional ecosystems and human socio-economic activities to climate change.

1.1 Objectives of the Study

The aim of this study is to evaluate the simulated and projected impacts of the SAOD on the regional rainfall variability using CMIP6 multi-model ensemble. This study focuses on the austral winter (June-August) when the SAOD variability is most pronounced. To achieve this aim, the specific objectives are as follows:

- To analyze the SAOD-regional rainfall relationship in observations and CMIP6 multi-model ensemble of historical simulation.

• To evaluate the CMIP6 ensemble for the land regions where the observed SAOD impact on regional rainfall is particularly strong.

• To quantify the future SAOD-regional rainfall relationship under increasing greenhouse forcing.

2. Literature Review

2.1 Modes of Variability in the South Atlantic

The South Atlantic Ocean (SAO) exhibits several modes of variability that are expressed as anomalous oceanic and atmospheric conditions. These modes serve a crucial function of influencing the regional climate patterns, atmospheric pressure, rainfall, and wind circulation over the continental landmasses of Africa and South America.

Venegas et al. (1997) used Empirical Orthogonal Function (EOF) and Singular Value Decomposition analyses to investigate the independent and coupled variability of the Sea Level Pressure (SLP) and SST of the South Atlantic region (defined as 0° - 50°S, 70°W – 20°E). Their results identified three modes of coupled atmosphere-ocean variability in the South Atlantic with time periods of 14-16 years, 6-7 years and 4 years, respectively. The first mode of coupled variability was marked by an oscillation in the strength of the St. Helena anticyclone, followed by a dipole structure with north-south orientation in the SST anomalies, representing the SAOD. This dipole structure was said to originate from wind-related processes triggered by changes in the anticyclone and was found to be strongest in the austral summer (Morioka et al., 2011; Venegas et al., 1997). The second mode was defined by a zonal (east-west) displacement of the anticyclone after which large fluctuations of SST occurred over a broad area of the South Atlantic, off the coast of Africa. The authors noted that the SLP-SST coupling in this mode was weaker even though the SST changes seemed to trigger responses in the atmospheric circulation. The third mode identified by Venegas *et al*. (1997) was characterized by a relatively higher frequency (occurring at inter-annual scales - 4 years), marked by a north-south displacement of the anticyclone. This had a 1-2months lead on latitudinal fluctuations of SST over the central South Atlantic Ocean. This mode was also found to be strongly associated with the El Niño-Southern Pacific Oscillation (ENSO) (Venegas *et al*., 1997).

Sterl & Hazeleger (2003) described how modes of variability in the SAO form and decay. They implicated atmospheric variability as the main mechanism generating large-scale SST anomalies in the South Atlantic. Atmospheric pressure anomalies (i.e. changes in the anticyclone) trigger anomalous winds which in turn generate the SST anomalies through latent heat flux and mixed layer deepening (Sterl & Hazeleger, 2003). In another study, focusing on interannual scales, Trzaska *et al*., (2007) expanded their domain of analysis to

include the equatorial Atlantic. They identified a leading mode of zonal SST anomaly in the equatorial Atlantic. A second mode of SST anomalies representing a dipole in the subtropical Atlantic was also identified – similar to the findings of Venegas et al. (1997). The leading mode of zonal SST anomalies in the equatorial Atlantic is the dominant mode of tropical Atlantic variability in the austral winter (JJA) known as the Atlantic Niño (Keenlyside & Latif, 2007; Okumura & Xie, 2004; Xie & Carton, 2004; Zebiak, 1993). Its peak phase is marked by a relaxation of the southeast trade winds and zonally oriented anomalous warming along the Atlantic cold tongue region (3°S – 3°N, 20°W - 0°E).

The Benguela Niño is another mode of variability that manifests itself as anomalous warming off the coast of Angola [20°S – 10°S, 8°E – 15°E] and peaks in austral fall (March-April-May; MAM). Lübbecke et al. (2010) examined the Atlantic Niño and the Benguela Niño and found a robust linkage between the two modes. Specifically, the formation of positive SST anomalies off the coast of Angola leads the Atlantic Niño by 1– 3 months. They concluded that both events were results of the same processes; however, the Benguela Niño usually occurred before the Atlantic Niño due to differences in the seasonal changes of thermocline depth in the two regions. The authors therefore suggested that both events be treated as one, and called it the Eastern Tropical Atlantic Niño (Lübbecke et al., 2010).

The EOF analyses of SST in the South Atlantic carried out by Venegas et al., (1997) and Sterl & Hazeleger (2003) identified two SST EOF modes consisting of a monopole (first mode) and a dipole (second mode). Sterl & Hazeleger (2003) pointed out that this dipole mode in the second EOF was likely an artifact of the EOF technique and merged it with the first mode for their analyses. Nnamchi & Li (2011) argues that this dipole mode is actually a real occurrence and a major mode of variability in the South Atlantic, with the northeastern and southwestern parts of the basin significantly negatively correlated. This anti-correlation peaks in the austral winter irrespective of the dipole index (Morioka et al., 2011; Nnamchi et al., 2011) used so that the various definitions may indeed represent aspects of the same phenomenon (Nnamchi et al., 2017).

2.2 SAOD versus SASD

SAOD is the leading mode of coupled ocean-atmosphere variability in the South Atlantic with a domain within 5°N - 45°S (latitude) and 60°W – 20°E (longitude). It occurs when sharply contrasting SST anomalies persist between the northeastern (equatorial) and southwestern regions of the SAO. The centres of action of this opposite polarity in the SAO

appear off the coast of central equatorial Africa/West Africa and off the coast of Argentina–Uruguay-Brazil (see Fig 1) (Nnamchi et al., 2016; Nnamchi & Li, 2011). During the positive (negative) phase, there is above-the-average warming (cooling) in the northeast and below-the-average cooling (warming) in the southwest. The SAOD peaks in the austral winter (JJA) and tends to occur every 3-5 years (Nnamchi *et al*., 2016).

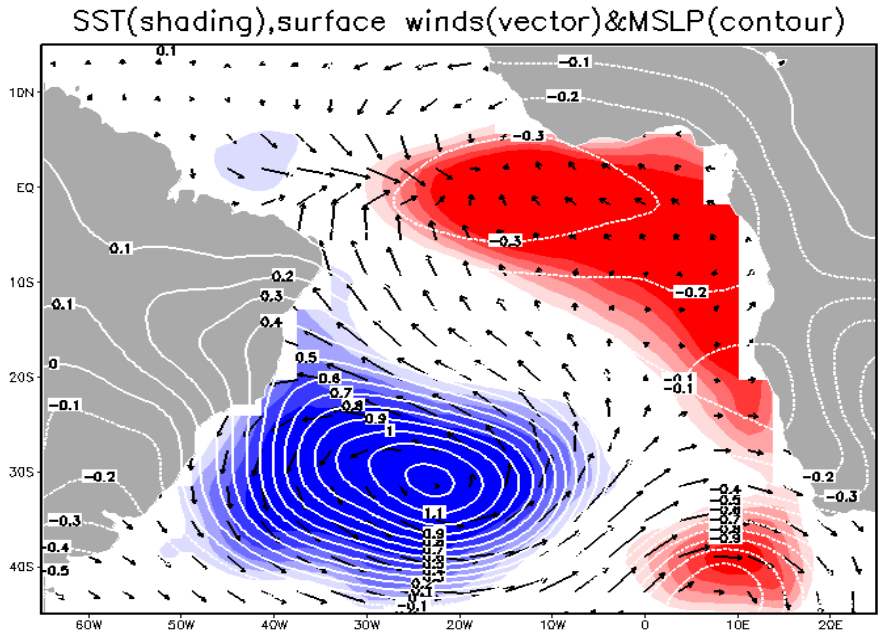

Figure 1: Sea surface temperature (RED, warming; BLUE, cooling), mean sea level pressure (contours) and surface wind anomalies (vectors) associated with the SAOD (from (Nnamchi et al., 2011).

Another major dipole mode of SST variability in the SAO is the SASD. It has a similar northeast-southwest orientation as the SAOD but exists in the more southwards and subtropical region (10° - 50°S; 60°W – 20°E). The northern arm of the SASD is generally positioned away from the equator, approximately within the range of 15-25°S (Morioka et al., 2011, 2014) but its southern arm falls within the domain of the SAOD. The SASD peaks in austral summer (Morioka et al., 2011; Nnamchi et al., 2017; Trzaska et al., 2007; Venegas et al., 1997) and is associated with a strengthening of the anticyclone. Notably, the SASD does not align with the Atlantic Niño in terms of seasonality and spatial distribution (Nnamchi et al., 2016).

The SAOD and SASD have been shown to be closely correlated; both indices are also strongly correlated with the Atlantic Niño (Nnamchi *et al*., 2017). A strong correlation between the SASD and ENSO has been detected in austral summer while this was not found

for the SAOD during the satellite era (Morioka *et al*., 2011; Nnamchi *et al*., 2017). Therefore, despite the robust correlation between the two modes, each may better capture different aspects of climate variability and teleconnections in the South Atlantic (Nnamchi et al., 2017).

2.3 Impacts of South Atlantic variability on Regional Climate

A strong correlation between the SAOD and rainfall over West Africa, particularly the Guinea coast, has been identified in the literature (Camberlin et al., 2001; Nnamchi et al., 2013; Nnamchi & Li, 2016). Nnamchi and Li (2011) found the positive (negative) phase of the SAOD to be associated with an increase (decrease) in rainfall over the Guinea Coast (Nnamchi & Li, 2011, 2016). In a study that involved the use of satellite-derived daily rainfall data and climate model experiments, Williams et al. (2008) show that anomalous cold SSTs in the central South Atlantic and warm SSTs off the coast of southwestern Africa were statistically related to rainfall extremes in southern Africa. They attributed the connection to local effects (such as increased convection) and remote effects (such as adjustment of the Walker-type circulation) (Williams et al., 2008).

Bombardi et al. (2014b) examined the relationship between the South Atlantic Dipole (SAD) and rainfall over eastern South America. Their analyses reveal that variations of SST in the South Atlantic, related to the SAD, impacts daily rainfall over eastern South America, through its influence on the positioning and movement of extratropical cyclones. These in turn influence the organization of the SACZ such that negative (positive) SAD events resulted in an increase (decrease) of rainfall over the southeast coast of Brazil. SASD is known to be a good indicator of rainfall variability in South America (Wainer et al., 2021), and Southern Africa (Morioka et al., 2011). Wainer et al. (2021) averred that while SASD plays a crucial role in rainfall variability in South America, meltwater forcing from retreating North Atlantic ice sheets and from Southern and Northern Hemisphere sources were the dominant drivers of SASD variability.

The foregoing is evident that a coupled ocean-atmosphere anomalous event in the South Atlantic has considerable influence on regional climate, particularly rainfall.

2.4 Modeling of the South Atlantic modes of variability and their impacts

Robertson et al. (2003) forced an atmospheric global circulation model (UCLA-AGCM) with boundary conditions that included SST anomalies from the South Atlantic. Their results demonstrated that both cold and warm SST anomalies in the SAO can have significant

impacts on atmospheric circulation and rainfall patterns. In particular, cold anomalies occurring in austral summers result in dipolar anomalies that bear resemblance to the SACZ. Conversely, warm anomalies on a basin-wide scale exert the most significant influence during austral winters, giving rise to equatorial baroclinic responses and fostering positive rainfall anomalies over the equatorial Atlantic Ocean. They also pointed out that the South Atlantic SST dipole pattern observed by Robertson & Mechoso (2000) did not affect the simulated SACZ and related circulation and rainfall anomalies

On the other hand, Haarsma et al. (2003) conducted simulations using the SPEEDY general circulation model. They introduced prescribed positive SST anomalies in the tropical regions and negative SST anomalies in the extratropics. Their results showed a southward shift of the ITCZ in northeast Brazil, accompanied by a notable increase in rainfall. This is inline with several observational studies (e.g, Bombardi & Carvalho, 2011; Moura & Shukla, 1981). They also found an increase in rainfall over the marine SACZ region, which is inconsistent with observational results (Bombardi & Carvalho, 2011; Robertson & Mechoso, 2000). Bombardi et al. (2014b) used the RAMS regional atmospheric model (Pielke et al., 1992) to perform numerical simulations of the SACZ forced with the SAD SST and atmospheric anomalies. They found that SACZ rainfall variability associated with SAD largely depended on atmospheric variability rather than on SST variability.

Nnamchi et al. (2017) found that the CMIP3/5 coupled models were able to replicate the strong association between the SASD and SAOD indices that had been observed. They reported that in all seasons, 54 of the 63 different CMIP3/5 models examined exhibited significant coefficients at the 99% confidence level. The authors however noted that the observed amplitudes in the Benguela-equatorial Niño region were better represented by the multi-model mean SST anomalies linked with the SAOD index.

The preceding section highlights numerous studies that apply global climate models, as well as regional climate models, to understand the dynamics and processes of the South Atlantic modes of variability and consequent impacts on climate. So far, we are not aware of any assessment of the CMIP6 simulation of the SAOD and its impacts on regional rainfall. This study aims to bridge this gap by considering historical and future simulations of the SAOD-regional rainfall relationship.

3. Materials and Methods

3.1 Study Region

The study site is the South Atlantic and the adjacent continents of Africa and South America. We further delineated the study areas over the continents on the basis of spatially-coherent correlations of grid-point rainfall with the SAOD index in observations (section 4.2). We have two delineated regions in Africa namely the Guinea Coast [13° - 5°N, 10°W-10°E], and Central Africa [5°N – 5°S, 10°-16°E] and two regions in South America namely the Northern Amazon [7°N – 5°S, 70°-50°W], and South East Brazil [12° - 27°S, 56°-40°W]. These regions are marked in Figure 2.

The SAO is defined as the oceanic area between 60°W and 20°E of longitude and 5°N and 45°S of latitude (Nnamchi et al., 2011; Sterl & Hazeleger, 2003). It covers an area of 30-40 million km^2 depending on where the southern boundary is set (Muller-Karger, et al., 2017). The SAO is characterized by the presence of ocean currents and the subtropical high-pressure system. These systems play a crucial role in shaping the ocean and climate conditions of the basin and the adjacent continental regions.

The four continental regions analyzed are briefly described below.

- **Guinea Coast**

The Guinean Coast encompasses the coast of West Africa northwards to the fringes of the Sahel. Parts of the region receives rainfall throughout the year with two seasonal peaks in June and September. The Guinea Coast climate is influenced by the presence of the Atlantic Ocean, and the ITCZ, a low-pressure belt near the equator where trade winds from the northern and southern hemispheres converge. Locations to the south of the ITCZ mean position generally receive rainfall whereas locations to its north experience dryness. The West African Monsoon, which brings rainfall to the Guinea Coast during JJA season, is modulated by the ITCZ. Its beginning is marked by the rapid northward movement of the ITCZ, usually in May/June (Sultan & Janicot, 2003). The ITCZ moving across West Africa results in the replacement of dry, warm, and dusty Harmattan winds with moisture-laden cold south-westerlies from the tropical Atlantic (Raj et al., 2019).

The rainy season typically occurs from April to October. Average monthly rainfall can range from 50 to 300 mm depending on the location (Tano et al., 2023). Temperatures during the

rainy season generally range from 25 to 32 °C coupled with high humidity. The dry season typically spans from November to March, characterized by reduced rainfall and lower humidity levels. The dry season is associated with the influence of the Harmattan winds, which blow from the northeast and carry dry air from the Sahara Desert. These winds can bring dust and haze to the Guinea Coast region, impacting visibility. Temperatures during the dry season range from 24 to 30 °C (USAID, 2018).

The Guinea Coast region experiences relatively high humidity throughout the year, influenced by its proximity to the tropical Atlantic Ocean. As a result, the region is able to support the presence of rainforests and mangroves along the coast. This contributes to the lush vegetation and diverse ecosystems found in the region.

- **Central Africa**

Central Africa generally experiences a tropical climate with high temperatures and high humidity throughout the year. The region is characterized by two main seasons: a rainy season and a dry season. During the rainy season, which typically lasts from November to April, Central Africa receives abundant rainfall. The rain is often heavy and frequent, contributing to the dense rainforests and lush vegetation that are characteristic of the region. Temperatures remain relatively high, ranging from 24 to 32 °C, accompanied by high humidity. In the dry season, which usually spans from May to October, rainfall decreases significantly, and the region experiences drier conditions. However, some areas may still receive sporadic showers. Temperatures remain warm, ranging from 20 to 30 °C with slightly lower humidity compared to the rainy season (USAID, 2018).

- **Northern Amazon**

Tropical rainforest climate is typical of the Northern Amazon region of South America, which covers portions of Venezuela, Colombia, Guyana, Brazil, northern Ecuador, and northern Peru. The proximity of this location to the equator, the Amazon Basin, and the Atlantic Ocean all have an impact on its climate. The Northern Amazon experiences high temperatures throughout the year. Seasonal variation of temperature is relatively low with average temperatures ranging from 25 to 28 °C. However, temperatures can be slightly cooler at higher elevations.

The Northern Amazon has a distinct wet and dry season pattern. The wet season typically lasts from around November to April, coinciding with the austral summer. The Amazon

rainforest receives rainfall throughout the year, which contributes to its lush vegetation and immense biodiversity. Monthly rainfall totals can range from 170 to 325 mm or more, depending on the specific location (Ronchail et al., 2002). Even during the dry season, some areas may still receive sporadic showers. Humidity is consequently lower in the dry season.

The rainforest and the Amazon River as well as its tributaries, are beneficial to the Northern Amazon region because they help control local climates and add to the region's overall wetness. Additionally, these rivers are essential in shaping the region's topography and sustaining its many different ecosystems (Foley et al., 2002).

- **South East Brazil**

A diverse range of climatic conditions characterize the Southeast region of Brazil. This is due to its extensive territory and varied topography. The region predominantly experiences a humid subtropical climate, with some areas transitioning into a tropical savanna climate in the northernmost parts. The climate is influenced by factors such as latitude, elevation, ocean currents, prevailing winds and the SACZ. The South East Brazil generally has four distinct seasons: summer, autumn, winter, and spring (Wiederhecker et al., 2002).

The summer generally lasts from December to February and is characterized by warm to hot temperatures and atmospheric high humidity levels. Average temperatures range from 25 to 30 °C in most areas, although some inland locations may experience higher temperatures. It is the wettest season, with frequent afternoon thunderstorms and periods of heavy rainfall. The autumn (March to May) brings milder temperatures as the summer heat begins to dissipate. Average temperatures range from 20 to 25 °C. Rainfall decreases compared to summer, but showers and occasional storms can still occur. The winter season lasts from June to August. Temperatures can vary widely depending on the specific location and elevation, ranging from 10 to 20 °C. Some areas at higher elevations or in the southernmost parts of the region may experience near-freezing temperatures. Winter is drier compared to other seasons, with lower rainfall totals and clearer skies. Spring (September to November) brings a gradual increase in temperatures as the region transitions into summer, with average temperatures range from 20 to 25 °C (Wiederhecker et al., 2002).

It is worth noting that the South East Brazil is known for its microclimates and localized variations due to its diverse topography. Maritime influence is strong in coastal areas, with milder temperatures and higher humidity levels, while greater temperature fluctuations and lower humidity, persist in the inland areas.

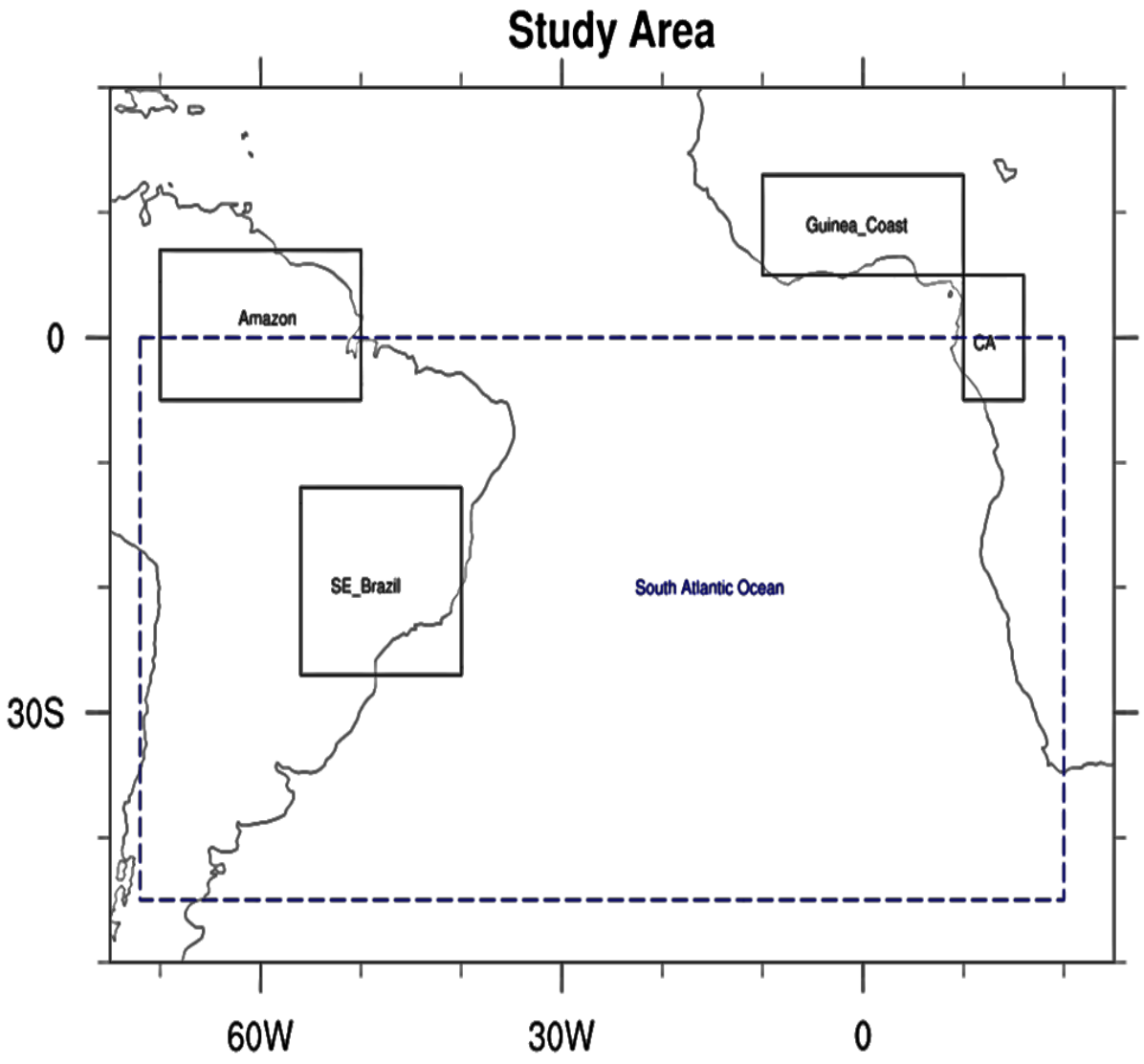

Figure 2: Map of study area indicating the four (4) regions in the South Atlantic considered (black boxes). [CA = Central Africa, SE_Brazil = South East Brazil]. Oceanic region of the South Atlantic is enclosed in dashed box.

3.2 Data collection and description

- **Sea Surface Temperature (SST) Observations**

For the historical analyses, global SST data from 1940 to the present was obtained from the Hadley Centre Global Sea Ice and Sea Surface Temperature (HadISST) analysis archive (Rayner, 2003; Rayner et al., 2006) available at 1° longitude by 1° latitude resolution. The dataset consists of monthly mean SST, the unit is °C. The data file was downloaded from the UK Met Office Hadley Centre website[2].

2 https://www.metoffice.gov.uk/hadobs/hadisst/data/download.html.

◆ **Rainfall data Observations**

Observations rainfall data was obtained from the Global Precipitation Climatology Centre (GPCC, version 2022), a full data monthly product containing global land-surface rainfall based on the ~86,000 stations world-wide that feature record durations of 10 years or longer. Rainfall anomalies at the stations are interpolated and then superimposed on the GPCC Climatology V2022 in the corresponding resolution. The temporal coverage of the dataset ranges from January 1891 until December 2020. Although this data is available at various resolutions, we selected the 1º × 1º spatial resolution for this study. The Full Data Monthly Product is updated at irregular time intervals subsequent to significant database improvements (Schneider et al., 2022). The data was obtained from the Deutscher Wetterdienst (DWD, National Meteorological Service of Germany) website[3].

◆ **CMIP6 Ensemble**

This study analyzed historical SST and rainfall simulated datasets from CMIP6 models' simulations. We simply selected 44 models that have both variables in the historical archive. Out of this number, 35 of the models that archived the two variables for the Shared Socioeconomic Pathway (SSP585) were selected for the analysis of the projected SAOD-regional rainfall variability.

The future simulation scenario considered (SSP585) refers to a high-emission pathway where greenhouse gas emissions continue to increase throughout the 21st century without significant efforts to mitigate climate change. In this scenario, fossil fuels continue to dominate the global energy mix, and little progress is made in adopting sustainable practices or reducing greenhouse gas emissions (Riahi et al., 2017). This scenario is chosen because it represents a situation where there are high challenges to mitigation and adaptation, which is similar to current trends where global Green House Gas (GHG) emissions have been steadily increasing over the last decade (Bergquist et al., 2019; Ritchie et al., 2020).

The CMIP6 outputs were obtained from the German Climate Computing Centre (DKRZ) supercomputer database[4]. The list of models analyzed is shown in the table below (Table 1). The models are from different countries with varying spatial resolutions; hence they were re-mapped to a common grid of 1º × 1º spatial resolution.

3 https://opendata.dwd.de/climate_environment/GPCC/html/fulldata-monthly_v2022_doi_download.html

4 https://esgf-data.dkrz.de/projects/cmip6-dkrz/

The CMIP6 is the latest phase of an ongoing international effort to improve climate modeling and understand Earth's climate system organized under the auspices of the World Climate Research Programme's Working Group on Coupled Modelling. CMIP6 involves a collaborative endeavor by climate modeling centers worldwide to develop and run state-of-the-art climate models to simulate past, present, and future climate conditions. Each modeling group contributes their own model, which is based on a set of equations that describe various components of the Earth system, including the atmosphere, oceans, land surface, sea ice, and biogeochemical cycles (Eyring et al., 2016). CMIP6 models generally feature enhanced representations of Earth system processes, improved spatial resolutions, and updated parameterizations. The outputs of these models are made freely available to the scientific community and the public through data portals like the Earth System Grid Federation (Eyring et al., 2016). This open access policy encourages collaboration and enables researchers worldwide to analyze the model outputs, validate the models, and contribute to climate research.

Table 1: Information of the 44 CMIP6 models used to construct the analyzed ensemble

S/N	**Model name**	**Modeling institution**	**Horizontal resolution (Atmosphere, Ocean km)**	**Reference(s)**
1	ACCESS-CM2	CSIRO Commonwealth Scientific and Industrial Research Organisation Australia	140, 70 km	(Bi et al., 2020; Ziehn et al., 2020)
2	ACCESS-ESM1-5		140, 70 km	
3	AWI-CM-1-1-MR	AWI Alfred Wegener Institute Germany	80, 20 km	(Sidorenko et al., 2015)
4	AWI-ESM-1-1-LR		170, 50 km	(Semmler et al., 2020)
5	BCC-CSM2-MR	BCC Beijing Climate Centre, China	100, 80 km	(T. Wu et al., 2019)
6	BCC-ESM1		250, 80 km	(T. Wu et al., 2020)
7	CAMS-CSM1-0	CAMS Chinese Academy of Meteorological Sciences, China	100, 90 km	(Rong et al., 2018)
8	CAS-ESM2	CAS Chinese Academy of Sciences	100, 100 km	(Chai, 2020)

9	CanESM5	CCCMa Canadian Centre for Climate Modelling and Analysis Canada	250, 70 km	(Swart et al., 2019)
10 11	CESM2 CESM2-WACCM	NCAR National Center for Atmospheric Research USA	100, 60 km 100, 60 km	(Danabasoglu et al., 2020)
12 13 14	CMCC-CM2-SR5 CMCC-CM2-HR4 CMCC-ESM2	CMCC Centro Euro-Mediterraneo sui Cambiamenti Climatici Italy	100, 70 km 100, 70 km 100, 70 km	(Cherchi et al., 2018) (Scoccimarro et al., 2020)
15 16 17	E3SM-1-0 E3SM-1-1-ECA E3SM-1-1	E3SM National Laboratories Consortium, USA	100, 40 km 100, 40 km 100, 40 km	(Golaz et al., 2019)
18 19 20	EC-Earth3-AerChem EC-Earth3 EC-Earth3-CC	EC-Earth Consortium Europe	80, 70 km 120, 70 km 80, 70 km	(Döscher et al., 2022)
21 22	FGOALS-f3-L FGOALS-g3	CAS Chinese Academy of Sciences China	90, 80 km 190, 80 km	(He et al., 2020) (L. Li, 2020)
23	FIO-ESM-2-0	FIO-QNLM First Institute of Oceanography and Plot National Laboratory for Marine Science and Technology (Qingdao), China	100, 60 km	(Bao et al., 2020)
24 25 26	GISS-E2-1-G-CC GISS-E2-1-G GISS-E2-1-H	NASA-GISS Goddard Institute for Space Studies, USA	200, 100 km 200, 100 km 200, 100 km	(Kelley et al., 2020)
27	GFDL-ESM4	NOAA-GFDL National Oceanic and Atmospheric Administration, Geophysical Fluid Dynamics Laboratory USA	100, 20 km	(Dunne et al., 2020)
28	IITM-ESM	CCCR-IITM Centre for Climate Change Research, Indian institute of Tropical Meteorology, India	170, 90 km	(Swapna et al., 2018)
29 30	INM-CM4-8 INM-CM5-0	INM Institute for Numerical Mathematics Russian Federation	150, 70 km 150, 30 km	(Volodin et al., 2017, 2018)

31	IPSL-CM6A-LR	IPSL Institut Pierre-Simon Laplace France	160, 70 km	(Boucher et al., 2019)
32	KACE-1-0-G	NIMS-KMA National Institute of Meteorological Sciences, Korea Meteorological Administration Republic of Korea	140, 90 km	(J. Lee et al., 2020)
33	MCM-UA-1-0	University of Arizona, USA	260, 190 km	(Delworth. et al., 2002)
34	MIROC6	MIROC Consortium JAMSTEC, AORI, NIES, R-CCS Japan	120, 80 km	(Tatebe et al., 2019)
35	MPI-ESM1-2-HR	MPI-M Max Planck Institute for Meteorology Germany	80, 40 km	(Mauritsen et al., 2019; Müller et al., 2018)
36	MPI-ESM1-2-LR		170, 100 km	
37	MPI-ESM-1-2-HAM	HAMMOZ- Consortium Switzerland, Germany, UK, Finland	170, 100 km	(Neubauer et al., 2019)
38	MRI-ESM2-0	MRI Meteorological Research Institute Japan	100, 60 km	(Mizuta et al., 2012; Yukimoto et al., 2019)
39	NESM3	NUIST Nanjing University of Information Science and Technology, China	170, 70 km	(Cao et al., 2018)
40	NorCPM1	NCC NorESM Climate Modelling Consortium Norway	190, 60 km	(Guo et al., 2019; Seland et al., 2020)
41	NorESM2-LM		190, 60 km	
42	NorESM2-MM		100, 60 km	
43	SAM0-UNICON	SNU Seoul National University, Republic of Korea	100, 60 km	(Park & Shin, 2019)
44	TaiESM1	AS-RCEC Research Center for Environmental Changes, Academia Sinica Taiwan, China	100, 60 km	(W.-L. Lee & Liang, 2020)

(source: https://www.ipcc.ch/report/ar6/wg1/downloads/report/IPCC_AR6_WGI_AnnexII.pdf)

3.3 Data analyses

- **The Analysis periods**

Two time periods are considered in this study – the historical and SSP585 projection periods. The historical period (1950 – 2014) spans 65 years. Data coverage of the ocean and atmosphere, particularly for the South Atlantic, improved after the second World War (Woodruff et al., 1987, 2005). Hence 1950 has been widely used as a suitable starting point for historical simulations (Ajibola et al., 2020; Gulev et al., 2021). 2014 is the last year for historical simulations in CMIP6 models hence its adoption here (Eyring et al., 2016). A similar 65 years is considered for the SSP585, starting from 2015 to 2079. This was done to ensure the analyses in both periods were adequately comparable.

- **Calculation of the SST and rainfall anomalies**

All the datasets analysed consist of monthly means. To define the monthly anomalies, firstly for each dataset, the monthly climatology was computed. The period used for the climatology is 65 years; 1950 - 2014 period for the historical simulations, and 2015 – 2079 for the SSP585 scenario. Then, the monthly anomaly was computed for each grid-point as the difference between the climatology and the monthly value for each year in both scenarios (see Equation 1). Prior to subsequent analyses, the anomalies for the austral winter were calculated by averaging the monthly means for JJA, the season during which the SAOD exhibits maximum variability.

$$x' = x_i - \bar{x} \qquad \text{(Eq. 1)}$$

Where;

- x' is the anomaly
- x_i represents the monthly values for January to December
- $\bar{x}$ is the climatological-mean for each month.

The anomalies were then detrended – that is the long-term trends were removed in order to focus on the interannual variability. Detrending is performed to distinguish between the natural variability of a climate signal and any underlying trend caused by factors such as climate change or external forcings (Z. Wu et al., 2007). By removing the trend, we could analyze the anomalies and patterns of variability.

◆ **Definition of the SAOD Index**

The SAOD index (SAODI) is defined as the normalized difference between the domain-averaged SST anomalies over the North East Pole (NEP) and the domain-averaged SST anomalies over the South West Pole (SWP) of the South Atlantic as follows:

$$SAODI = [SSTA]_{NEP} - [SSTA]_{SWP} \qquad \text{(Eq. 2)}$$

Where;

- NEP is defined as the region [10°E–20°W, 0°–15°S]
- SWP is defined as the region [10°– 40°W, 25°– 40°S]
- the square brackets denote area-averages, and the subscripts (NEP and SWP) denote the domains over which the averages were computed. These regions are shown in Fig. 3.

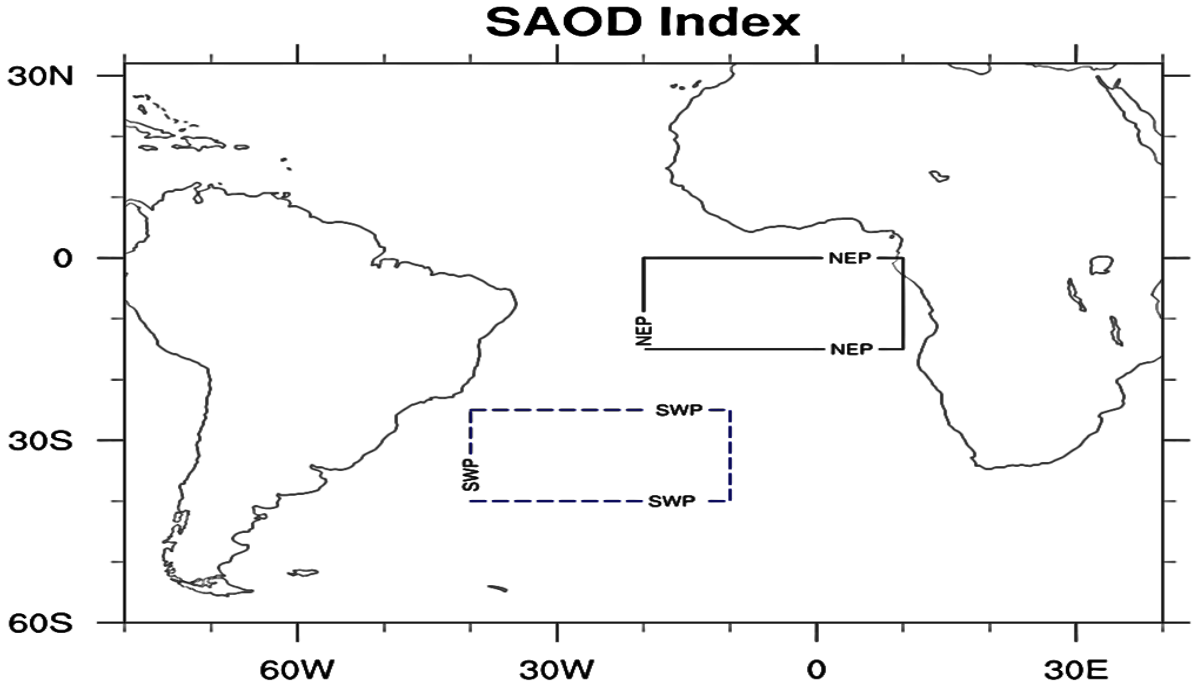

Figure 3: Geographical location of the North East Pole (black solid box) [NEP; 10°E–20°W, 0°–15°S] and South West Pole (blue dashed box) [SWP; 10°– 40°W, 25°– 40°S] used to calculate the SAOD index.

This index serves as an appropriate numerical representation of SAOD events for each year under consideration. Positive (negative) values of the SAODI indicate warming (cooling) in the NEP and cooling (warming) in the SWP. The SAODI was calculated from the SST observations and the CMIP6 models, respectively. It was calculated for the austral winter

season of the years under consideration for both the historical (1950 – 2014) and future (2015 – 2079) scenarios.

- **Regional rainfall indices**

First, correlation analysis was performed between the SAOD index and global rainfall map during JJA using the observational datasets. Statistically significant correlations were found over parts of Africa and South America. Thus, we defined four regions of spatially-coherent significant SAOD-rainfall correlations viz: Guinea Coast, Central Africa, Northern Amazon and South East Brazil. Rainfall indices were calculated for these four regions as the domain-averaged rainfall anomalies for the periods under consideration - historical (1950 – 2014) and SSP585 (2015 – 2079).

- **Correlation Analyses**

The observations and modeled SAOD-rainfall relationship was analyzed using the Pearson correlation analysis. The correlations were performed between the SAOD index and rainfall in two phases. Firstly, the SAODI was correlated with global rainfall anomalies to identify regions of significant correlation ($p \leq 0.05$) within the adjacent land areas of the South Atlantic. This was done for both observations and the CMIP6 outputs. Secondly, we performed correlations between the SAODI and rainfall indices in these regions.

This analysis allows us to quantify the strength of the relationship or association between the SAOD and rainfall. The correlation coefficients (r) show how much variability in rainfall over parts of Africa and South America is related to variability in the SAOD and is given by;

$$r = 1 - \frac{\sum_{i=1}^{n}\left(x_i - \bar{x}\right)\left(y_i - \bar{y}\right)}{\sqrt{\sum_{i=1}^{n}\left(x_i - \bar{x}\right)^2 \sum_{i=1}^{n}\left(y_i - \bar{y}\right)^2}} \qquad \text{(Eq. 3)}$$

Where;

- x is the SAOD and y is the rainfall anomaly
- $\bar{x}$ and $\bar{y}$ are arithmetic means of both variables.

Correlating atmospheric variables with SST is a convenient method of demonstrating the impacts of SAOD on rainfall anomalies. The correlation coefficient generally ranges between -1 and +1, indicating the strength and direction of the relationship. A positive correlation ($r >$

0) shows that as the SAOD increases, the rainfall anomalies also increase over the continents. A negative correlation ($r < 0$) implies that as SAOD increases, rainfall decreases indicating an inverse relationship between the two variables. Where $r = 0$, it means there is no linear relationship between the two variables. This method has been used in several studies to investigate the relationship between ocean patterns and climate variability (Alhamshry et al., 2019; Nnamchi et al., 2017; Polo et al., 2008).

We conducted hypothesis testing to determine the statistical significance of the correlations. The null hypothesis for these tests (H_0) is that there is no correlation between the SAOD and rainfall anomalies over the adjacent land areas of Africa and South America. The alternative hypothesis (H_1) is that a correlation exists between the SAOD and rainfall in the regions under consideration. We set the *p*-value at 0.05 (95% confidence level) therefore where $p<0.05$, the null hypothesis is rejected and the alternative hypothesis is accepted.

- **Regression Analyses**

We also used regression analysis to determine the response of rainfall anomalies over the adjacent continents to SAOD variability. The regression analysis was performed with the two indices (SAODI and rainfall), with the normalized SAODI as the independent (explanatory) variable and the rainfall indices as the dependent (response) variable. The resulting regression coefficients show how much the rainfall changes in mm/day over the four regions selected (Guinea Coast, Amazon, Central Africa, and South East Brazil) in response to a unit standard deviation in the SAOD. The regression equation is given as:

$$\hat{y} = \alpha + \beta x \qquad \text{(Eq. 4)}$$

Where;

- x is the SAOD, ŷ is the predicted rainfall anomaly for a unit standard deviation of x;
- β is the slope (the amount by which rainfall (y) changes for every unit change in SAOD (x)) given as:

$$\beta = \frac{n\left(\sum x_i y_i\right) - \left(\sum x_i\right)\left(\sum y_i\right)}{n\left(\sum x_i^2\right) - \left(\sum x_i\right)^2} \qquad \text{(Eq. 5)}$$

- α is the intercept (the value of y when x = 0); given as:

$$\alpha = \frac{\left(\sum y_i\right)\left(\sum x_i^2\right) - \left(\sum x_i\right)\left(\sum x_i y_i\right)}{n\left(\sum x_i^2\right) - \left(\sum x_i\right)^2} \qquad \text{(Eq. 6)}$$

here n represents number of observations/datapoints.

◆ Data Analysis Tool (NCAR Command Language and Python)

The data analysis and visualization in this study was done using a combination of the NCAR Command Language (version 6.6.2) and Python programming language. The NCL is a powerful scripting language developed by the United States National Center for Atmospheric Research (NCAR) for data analysis and visualization in the field of atmospheric and oceanic sciences. NCL provides researchers and scientists with a comprehensive set of tools for processing, analyzing, and displaying large and complex atmospheric and oceanic datasets (Brown et al., 2012)

All the analyses and most of the visualization in this work was done by writing and running NCL scripts (the programming language only runs on Linux operating system) which combined data manipulation, statistical analysis, and visualization tasks into reproducible and efficient procedures in order to streamline the data analyses workflow. The Seaborn package in Python (Waskom, 2021) was also used for some of the visualization due to its intuitive procedure for producing scatter plots and other similar graphics.

4. Results

In this section we present the results of our analyses. The first segment shows the results of the SAOD-rainfall correlation for the historical period, comparing observations to the CMIP6 model simulations. The second segment presents the future projections of the SAOD-rainfall relationship using regression analyses with the historical and SSP585 ensemble.

4.1 Evaluation of the SAOD-rainfall relationship in CMIP6 historical ensemble 1950-2014

4.1.1 SAOD Timeseries from Observations and CMIP6 historical ensemble

Figure 4 shows the observations and CMIP6 ensemble mean normalized SAODI timeseries for the historical period under consideration (1950 – 2014). The index is constructed according to the descriptions in section 3.3. n observations, positive SAODI events are more pronounced for about 14 years (between 1962 and 1976), then negative SAODI events persist for about 8 years until the mid-1980s. A regular oscillation between positive and negative SAOD events is observed post mid-1980s, although there is generally a tendency for the index to be persistent in one phase for a few years. Post 2000s show a positive phase bounded by two negative phases (Fig. 4(a)). This multi-year variability may be explained by the fact that the SAOD index represents a difference in SST anomalies (over large areas of the northeast and southwest South Atlantic) so that high frequency variability has been partly filtered out. The ensemble mean SAODI timeseries indicates an underestimation of the positive phase of SAOD in the late 1960's in comparison to observations. Also, in contrast to observations, during the 2000s a negative phase is bounded by two positive phases in the model ensemble depiction (Fig. 4(b)). However, the model ensemble seems to capture the observed dominance of a negative phase from 1980 to 1990 and the dominance of a positive phase during the transition period of 1960 to 1970 (Fig. 4(b)).

The normalized SAOD timeseries for each CMIP6 model was also constructed for the historical period under consideration. The model depiction of the SAOD timeseries varies across each model (Fig. 5).

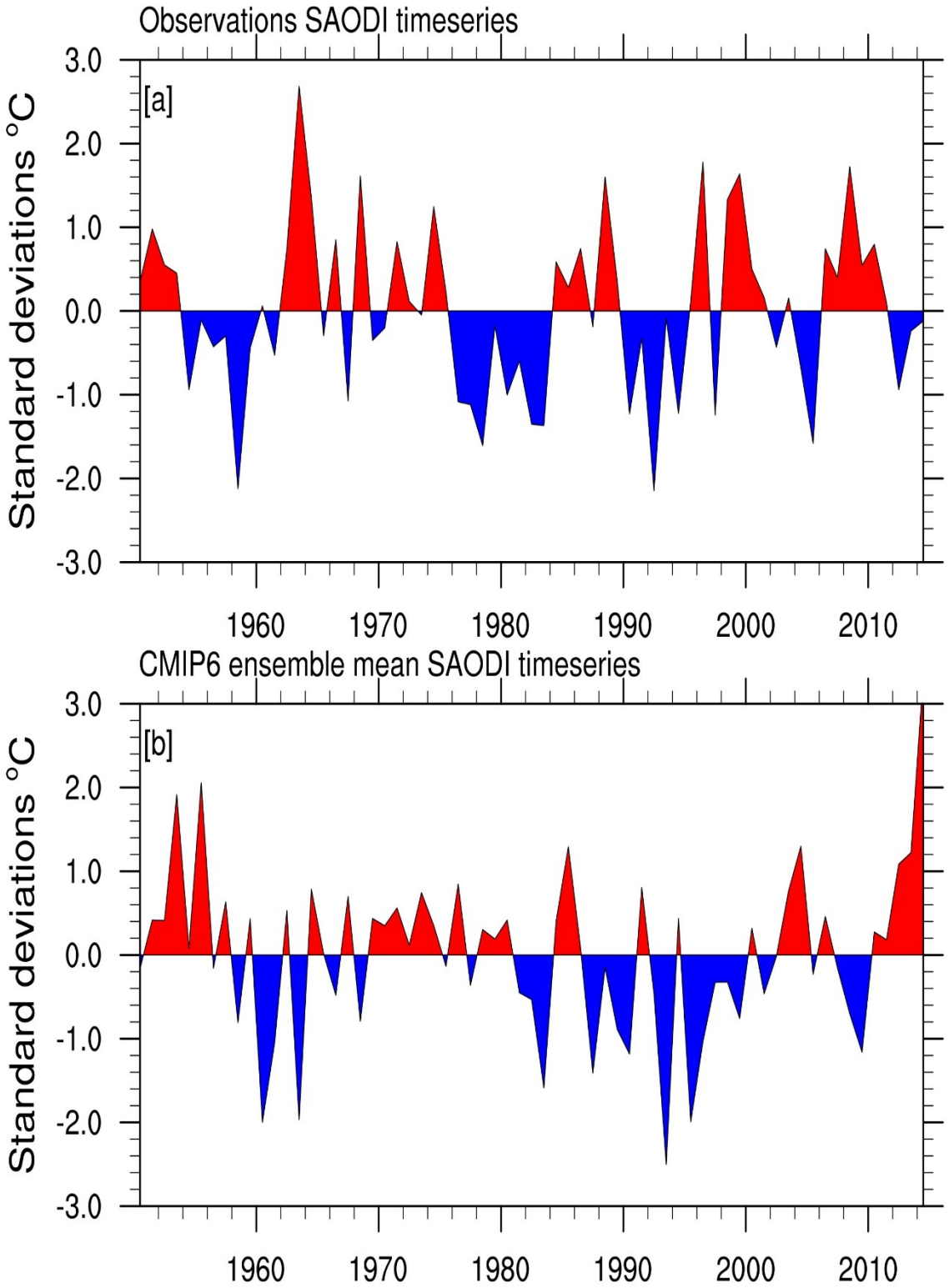

Figure 4: Normalized SAODI time series for JJA from observations (HadISST) data (a) and CMIP6 ensemble mean (b). Red troughs indicate positive phase of SAOD while blue troughs indicate negative phase of SAOD. Standard deviations in (°C)

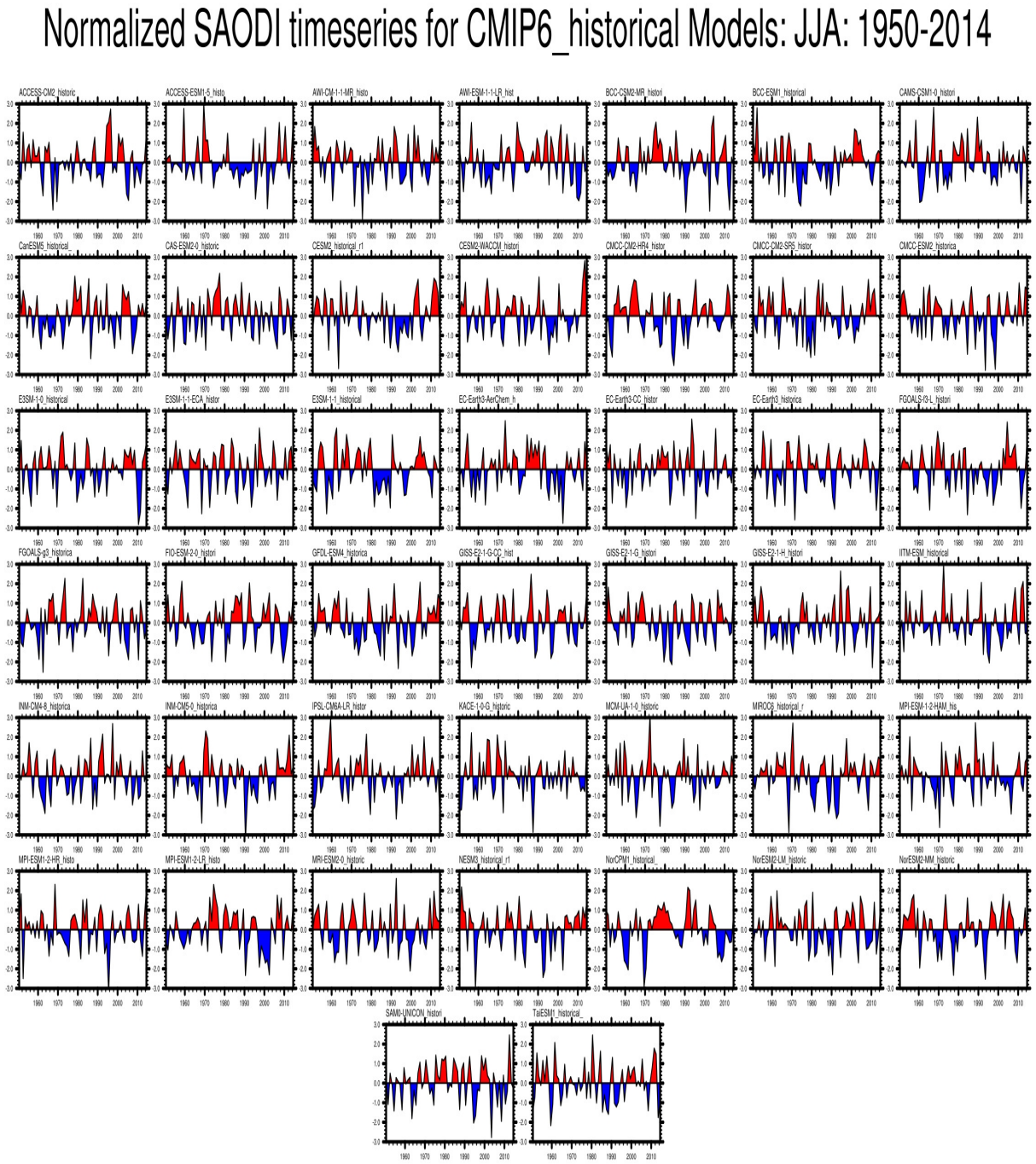

Figure 5: Normalized SAODI timeseries from CMIP6 model ensemble for the JJA season.

4.1.2 Relationship between the SAOD and Rainfall map in Observations and CMIP6 historical ensemble

The correlation between the SAODI and regional rainfall map using the observations dataset is shown in Figure 6. The pattern depicts statistically significant positive correlations over the Guinea Coast, Central Africa, and Northern Amazon, as well as significant negative correlations over South East and South of Brazil. This implies that the positive phase of the SAOD, with warm SST anomalies over the NEP, is associated with large-scale convergence and rainfall linked to the Atlantic ITCZ over the adjacent continental areas. On the other hand, the cold SST anomalies over the SWP off the Brazil-Uruguay-Argentina is associated with a significant reduction in rainfall over the SACZ, including South East and South of Brazil.

The spatial correlation maps for each of the 44 CMIP6 models analyzed for the historical period are also presented (Fig. 7). The models' depictions exhibit large variations from one another. Nonetheless, the multi-model mean bear some remarkable resemblance to the observed correlation map (Fig. 8). Specifically, the signs of the correlations similar over Central Africa, and Amazon; although the CMIP6 ensemble depicts overall weaker correlations than observations. The spatial extent of the simulated rainfall over the Guinea Coast is confined to the coastal fringes, while the observed negative correlation over the South East and South of Brazil is practically non-existent in the CMIP6 ensemble (Fig. 8).

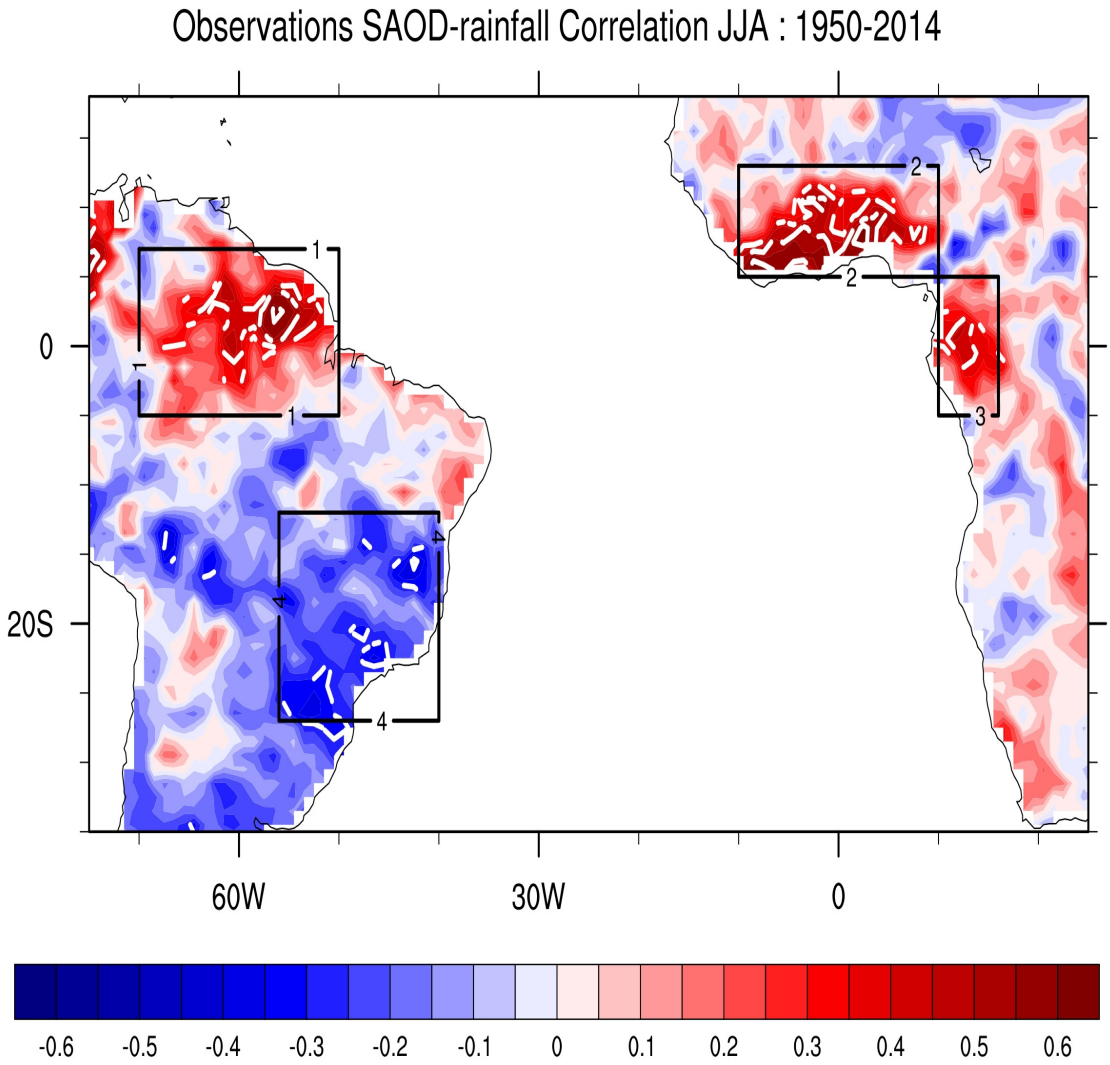

Figure 6: Spatial correlation (historical) of SAODI and rainfall anomalies (from observations data) in land regions adjacent to the South Atlantic. White contours represent areas with significant correlation ($p < 0.05$). Black boxes delineate regions of statistically significant correlation; 1 – Amazon, 2 – Guinea Coast, 3 – Central Africa, 4 – South East Brazil (SE_Brazil).

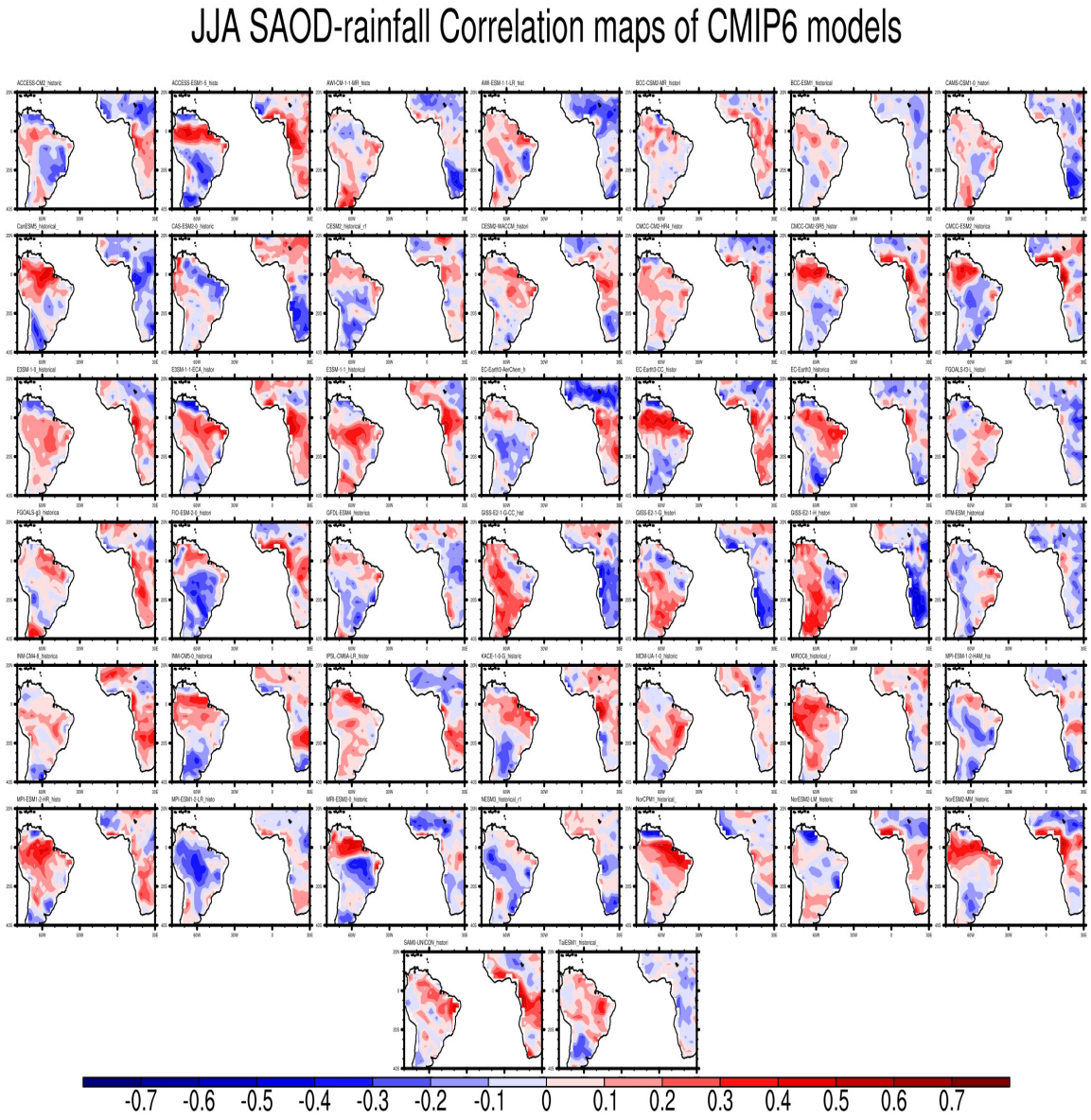

Figure 7: Spatial correlation of (historical) of SAODI and rainfall anomalies for individual CMIP6 models.

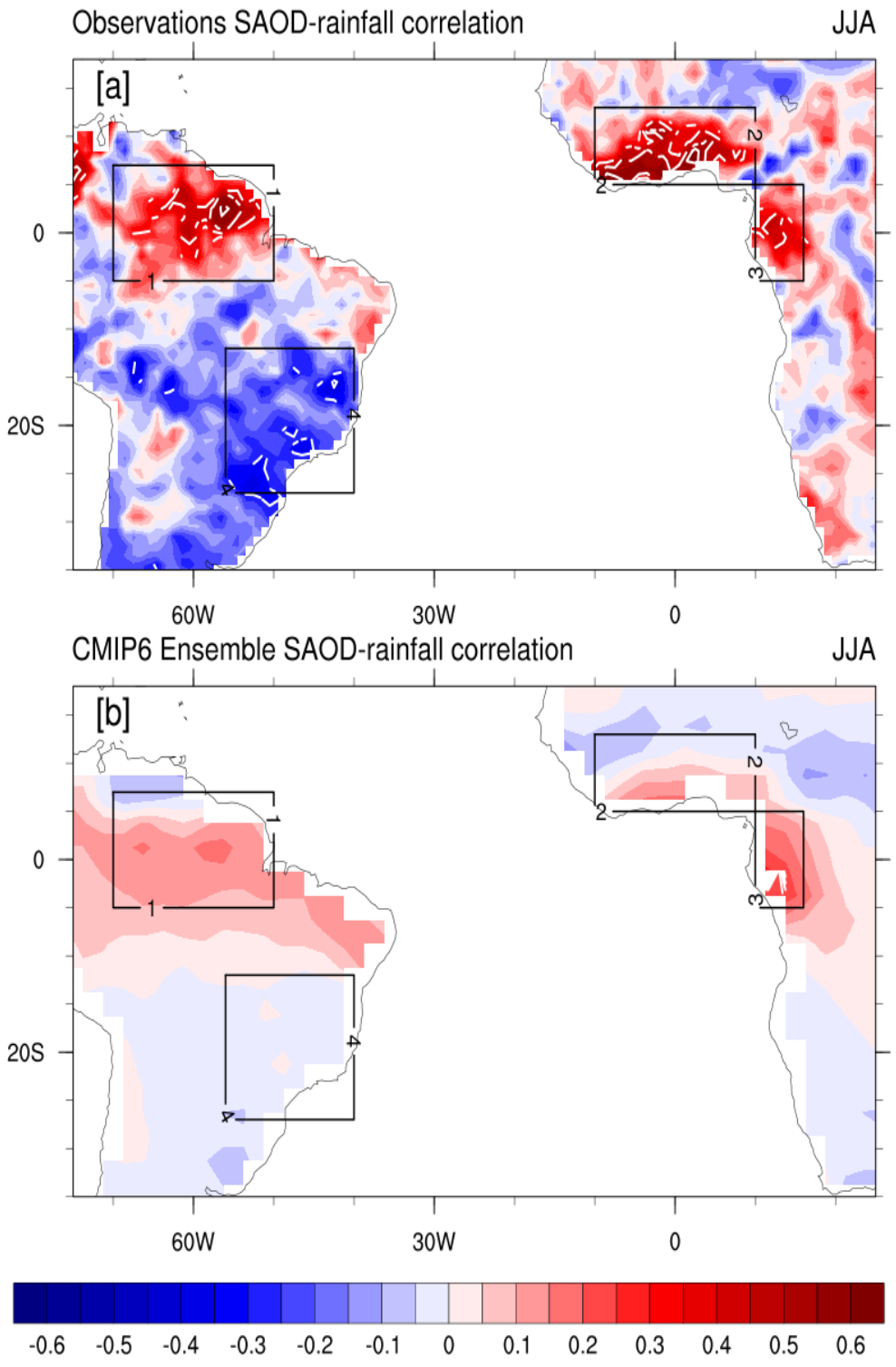

Figure 8: Correlation of SAODI and rainfall anomalies in JJA from observations (a) and multi-model mean (b). White contours indicate areas of statistically significant correlation while black boxes delineate the domains. 1 – Northern Amazon, 2 – Guinea Coast, 3 – Central Africa, 4 – South East Brazil (SE_Brazil).

4.1.3 Relationship between the SAODI and rainfall indices in the CMIP6 historical ensemble

Next, we assess the individual model performance in simulating the SAOD–rainfall correlation in each region delineated in section 4.1.2. Here we plot the correlation for each model against its p-value (Figures 10-13). The 95% confidence limit, ensemble-mean, and observational values are also indicated for reference. Here the ensemble mean was calculated in two ways for comparison: (i) an average of the correlation values of all models (mmm – green circle), and (ii) correlating the ensemble means of the SAODI, and rainfall anomaly time series (mmm2 – blue circle).

Northern Amazon

For Northern Amazon, the correlation in observation is positive (r = 0.48) and statistically significant ($p < 0.05$). 33 of the 44 models have the same sign of correlations as observations, whereas 11 models have a different sign (Figure 9). Of the 33 models that have the same sign as observations, only 15 models (34%) (MRI-ESM2-0, CMCC-CM2-SR5, IPSL-CM6A-LR, CanESM5, CMCC-ESM2, MPI-ESM1-2-HR, NorESM2-MM, INM-CM5-0, NorCPM1, FIO-ESM-2-0, EC-Earth3-CC, ACCESS-ESM1-5, EC-Earth3, MIROC6, GISS-E2-1-H) exhibit statistically significant correlations. Each multi-model means showed similar correlation signs to observations (positive) although not statistically significant ($p > 0.05$).

Guinea Coast

For Guinea Coast, the observation shows strong positive and statistically significant correlation (r = 0.59, $p < 0.05$). Seven of the 25 models that also have positive correlation are statistically significant – (FIO-ESM-2-0, CMCC-ESM2, NorESM2-LM, CMCC-CM2-SR5, ACCESS-ESM1-5, SAM0-UNICON, and NorESM2-MM). The second multi-model mean (mmm2) also shows statistically significant positive correlations. Notably, 19 models (43%) simulate a negative correlation ($r < 0$). The first multi-model mean had a weak positive correlation (Figure 10).

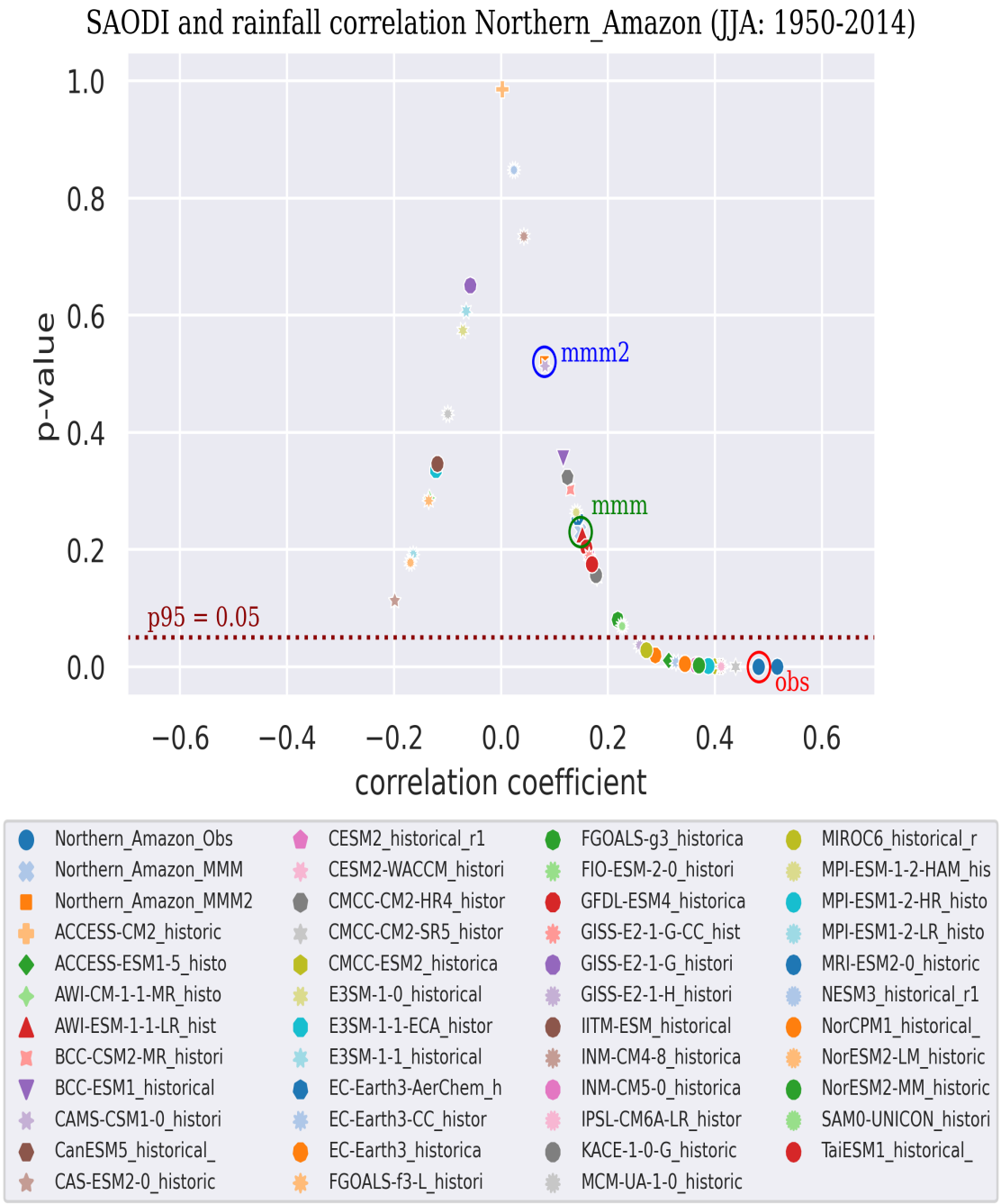

Figure 9: Scatterplot of correlation values (x – axis) against the significance level [*p* – value] (*y* – axis) of individual model simulation of SAODI-rainfall correlation in Northern Amazon region. Observation = Red circle, Multi-Model Mean; (mmm = green circle, mmm2 = blue circle). Horizontal dotted line is where *p* = 0.05. Data points at or below the horizontal line are statistically significant at 95% confidence level ($p \leq 0.05$).

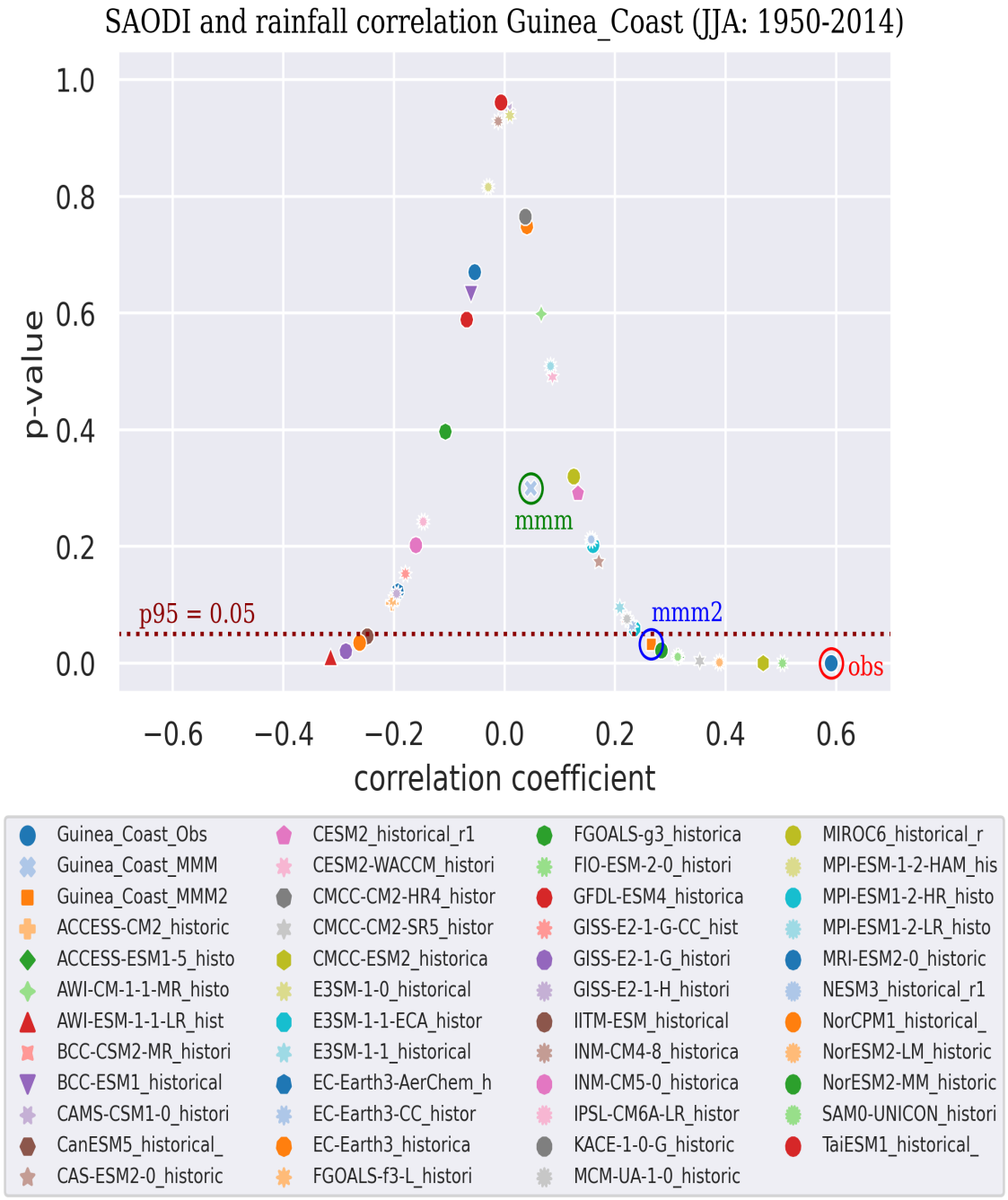

Figure 10: Scatterplot of correlation values (x – axis) against the significance level [p – value] (y – axis) of individual model simulation of SAODI-rainfall correlation in Guinea Coast region. Observation = Red circle, Multi-Model Mean; (mmm = green circle, mmm2 = blue circle). Horizontal dotted line is where p = 0.05. Data points at or below the horizontal line are statistically significant at 95% confidence level ($p \leq 0.05$).

Central Africa

For Central Africa, 23 of the 44 models (52%) and the second multi-model mean (mmm2) showed a statistically significant positive correlation ($r > 0$, $p < 0.05$) similar to observations ($r = 0.37$). However, 16 of them (E3SM-1-1, E3SM-1-1-ECA, ACCESS-CM2, E3SM-1-0, EC-Earth3-AerChem, INM-CM4-8, FGOALS-g3, KACE-1-0-G, EC-Earth3, FIO-ESM-2-0, CMCC-CM2-SR5, EC-Earth3-CC, CMCC-ESM2, SAM0-UNICON, ACCESS-ESM1-5, NorESM2-MM) overestimated the correlation ($r > 0.37$[Obs]) while the rest underestimate it. Of the six models that have an opposite sign of correlation, three of them (CanESM5, GISS-E2-1-G-CC, GISS-E2-1-H) are statistically significant ($p < 0.05$, $r < 0$) (Fig. 11).

South East Brazil

Observations showed a statistically significant negative correlation in this region ($r = -0.38$, $p < 0.05$). Only three models have a similar correlation, albeit underestimated (ACCESS-CM2, GFDL-ESM4, ACCESS-ESM1-5) (Fig. 12). 21 models (47%) and the second multi model mean (mmm2) show positive correlation signs in contrast to the observation, with three of these models (GISS-E2-1-G, MCM-UA-1-0, GISS-E2-1-G-CC) being statistically significant (that is $r > 0$ and $p < 0.05$). The first multi-model mean (mmm) has a weak negative correlation.

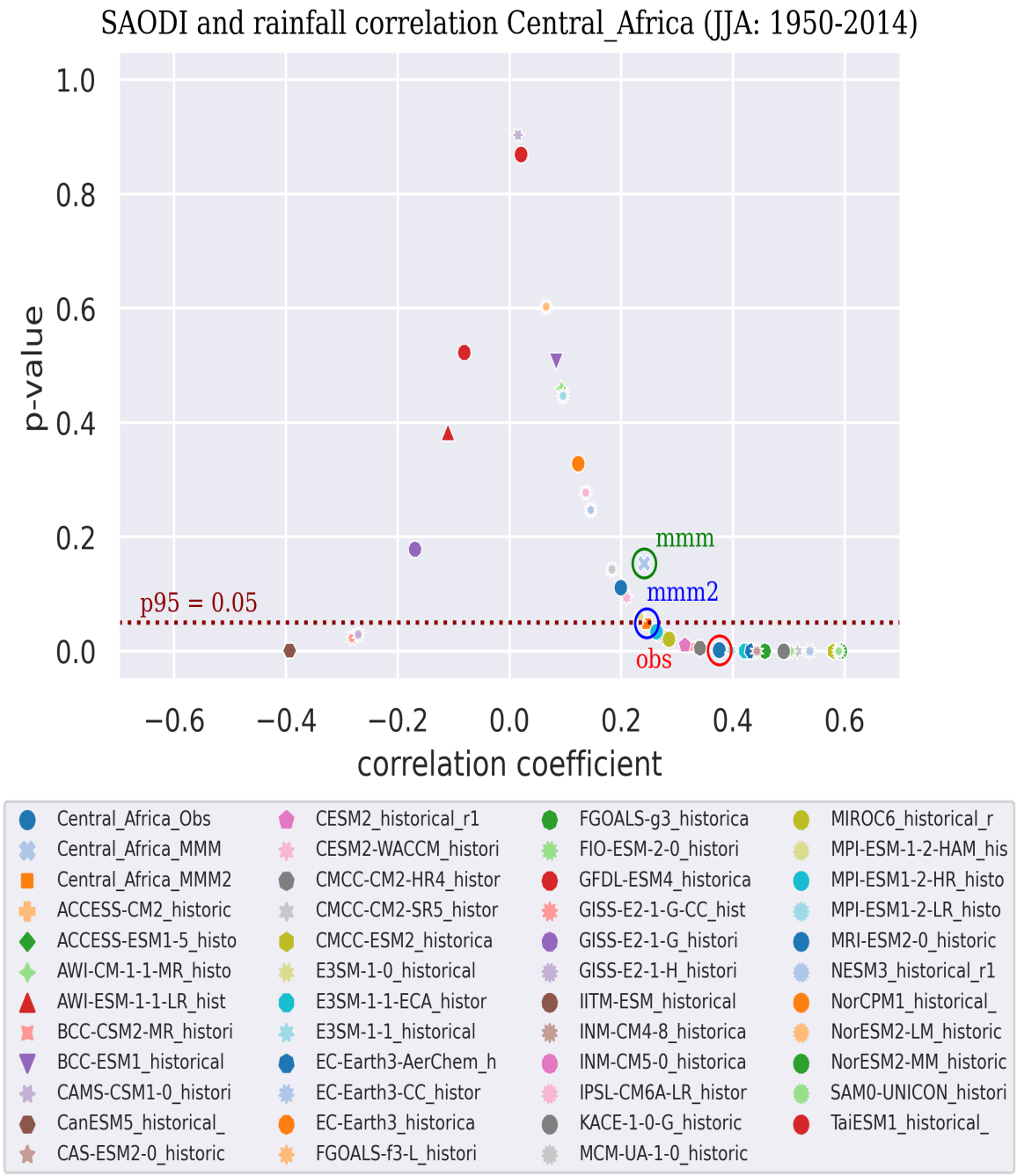

Figure 11: Scatterplot of correlation values (x – axis) against the significance level [p – value] (y – axis) of individual model simulation of SAODI-rainfall correlation in Central Africa region. Observation = Red circle, Multi-Model Mean; (mmm = green circle, mmm2 = blue circle). Horizontal dotted line is where $p = 0.05$. Data points at or below the horizontal line are statistically significant at 95% confidence level ($p \leq 0.05$).

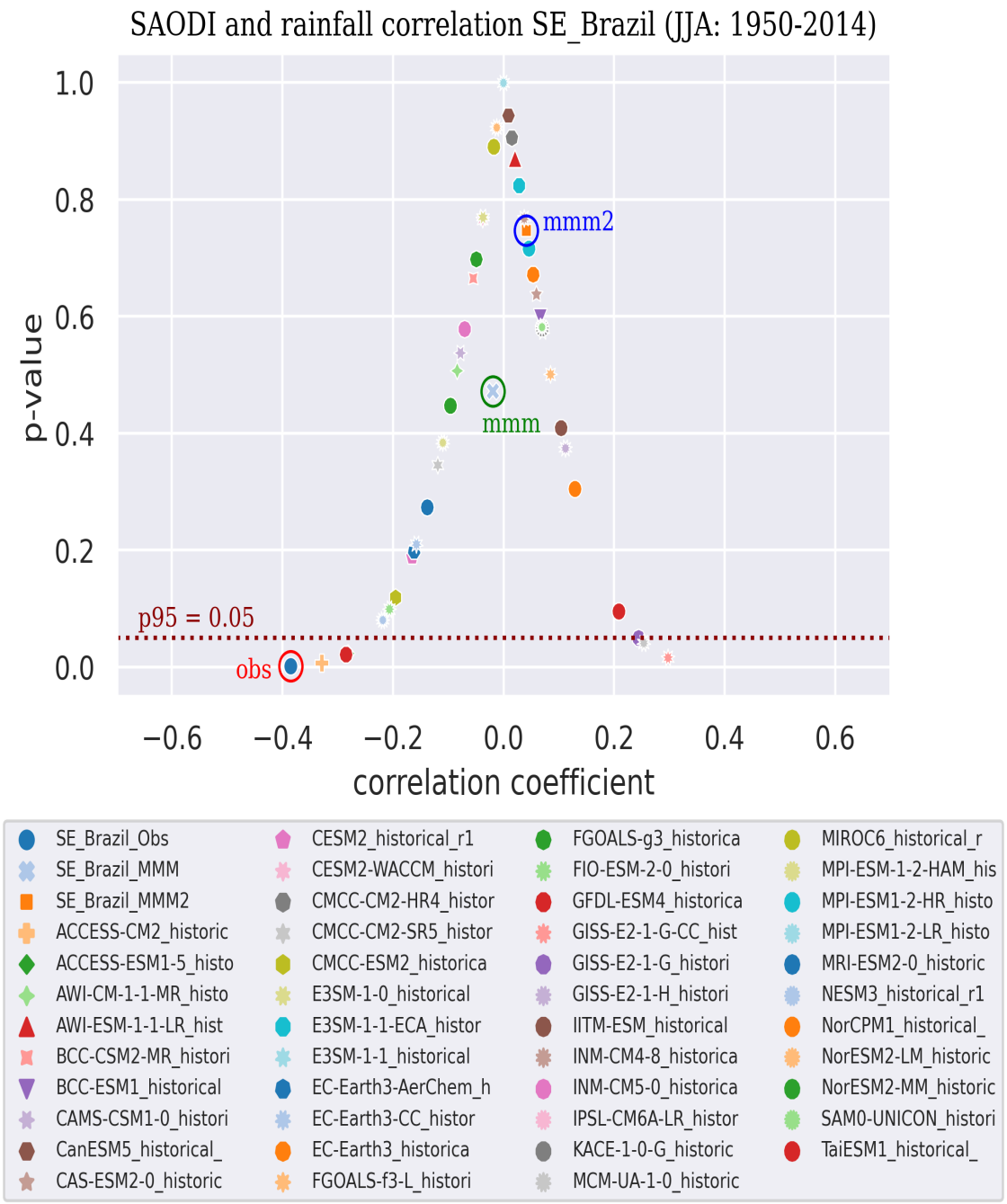

Figure 12: Scatterplot of correlation values (x – axis) against the significance level [p – value] (y – axis) of individual model simulation of SAODI-rainfall correlation in South East Brazil region. Observation = Red circle, Multi-Model Mean; (mmm = green circle, mmm2 = blue circle). Horizontal dotted line is where p = 0.05. Data points at or below the horizontal line are statistically significant at 95% confidence level ($p \leq 0.05$).

4.2 Projections of the SAOD-Rainfall relationship in CMIP6 SSP585 ensemble (2015-2079)

4.2.1 Spatial pattern of the projected SAOD-rainfall relationship

Next, we investigate the projections of the SST-rainfall relationship under SSP585. We choose this emission scenario because observations suggest that the current trajectory of greenhouse emission is consistent with the SSP585. Here we use 65 years (2015-2079) to allow a comparison with observations which also covers 65 years (1950-2014).

Regression analysis was performed to elucidate the influence of the SAOD on rainfall over Africa and South America. We used the SAOD as the explanatory variable and the rainfall anomalies as the response variable. For a comparison with the historical period, a similar analysis was also done using the CMIP6 historical ensemble. Here we use CMIP6 models that archived SST and rainfall for both the historical and SSP585 scenario.

The ensemble mean depiction of SAOD influence on rainfall is shown in Figure 13. The historical and SSP585 scenarios have striking similarities – SAOD has strong positive influence on rainfall anomalies over Northern Amazon, Guinea Coast and Central Africa. Notably, the positive influence of SAOD on rainfall in the Guinea Coast is confined to the coastal fringes. For South East Brazil, the ensemble mean simulation shows that SAOD influence over rainfall changes from negative, in the historical, to positive in the SSP585 scenario (Fig. 13 (b)). SAOD influence in this region is however much weaker in both scenarios. The difference map (Fig. 13 (c)) shows the models' depiction of future changes in the SAOD-rainfall relationship under the SSP585 scenario. Models simulate an increase of SAOD influence on rainfall over most parts of South America, while over Africa a decrease is prominent over Central Africa, however the Guinea Coast shows a slight increase over its western fringes.

Following is the analysis of individual model performance, comparing both scenarios with observations, in each region.

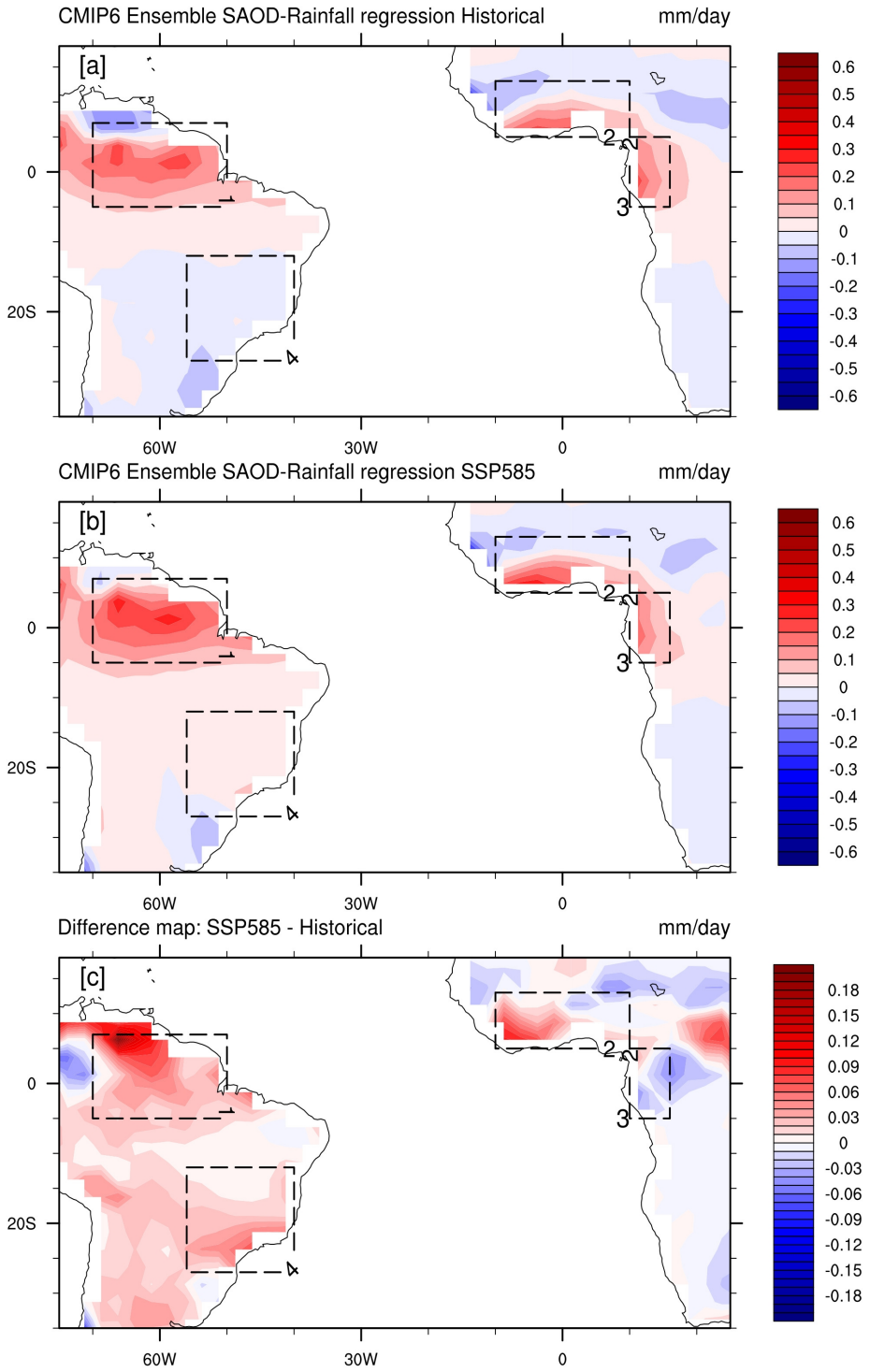

Figure 13: Regression of rainfall anomalies on SAODI from CMIP6 models for JJA in historical (top [a]) and SSP585 projection (middle [b]). Map of the difference between [a] and [b] is shown in [c]. Dashed boxes delineate the domains: 1 – Amazon, 2 – Guinea Coast, 3 – Central Africa, 4 – South East Brazil (SE_Brazil)

4.2.2 Projections of SAOD impact on the regionally-averaged rainfall

Northern Amazon

For Northern Amazon, the observed regression coefficient is $\beta = 0.31$ mm/day which denotes the magnitude of rainfall anomaly response to a unit standard deviation of the SAOD (Fig. 14). The historic simulations of MIROC6, NorESM-MM, ACCESS-ESM1-5, and CanESM5 are closest to observation however their future projections indicate a reduction in the rainfall anomaly forced by SAOD. Notably, two of the aforementioned models (ACCESS ESM1-5 and CanESM5), as well as MRI-ESM2-0, overestimate the rainfall response to SAOD in their historic simulations. On the other hand, the model future projections that come closest to observations (CESM2, CMCC-ESM2, GFDL-ESM4, MPI-ESM1-2-HR) all have historical simulations that underestimate the SAODI-rainfall relationship. Ten models (NorESM2-LM, CAS-ESM2-0, E3SM-1-1-ECA, AWI-CM-1-1-MR, MP-ESM1-2-LR, FGOALS-f3-L, IITM-ESM, E3SM-1-0, E3SM-1-1, GISS-E2-1-G) have a negative rainfall response in their historic simulations, while all but two models (AWI-CM-1-1-MR and MPI-ESM1-2-LR) have future projections with a positive sign (Fig. 14). Notably, the two multi-model means (mmm and mmm2) simulated an increase in rainfall response to SAOD under SSP585 scenario.

Guinea Coast

The observed magnitude of Guinea Coast rainfall response to the SAOD in this region is $\beta = 0.38$ mm/day. The models with historic simulations that come closest to observation (NorESM2-LM, CMCC-ESM2 and FIO-ESM-2-0) show an increase in rainfall anomaly forced by SAOD in their projected simulations (Fig. 15). Only one model (NorESM2-LM) overestimates its historic simulation of rainfall response to SAOD influence. 13 models show an inverse SAOD-rainfall relationship (negative coefficient, $\beta<0$) in their historical simulation; GISS-E2-1-G, FGOALS-f3-L, IITM-ESM, ACCESS-CM2, FGOALS-g3, MRI-ESM2-0, CanESM5, GISS-E2-1-H, INM-CM5-0, IPSL-CM6A-LR, GFDL-ESM4, INM-CM4-8, and TaiESM1. Of these, the first six show a similar negative regression in their projections while the last seven have future projections with positive sign albeit to varying degrees. Here the model ensemble mean (mmm) indicated an increase of SAOD influence on rainfall under SSP585 (Fig. 15).

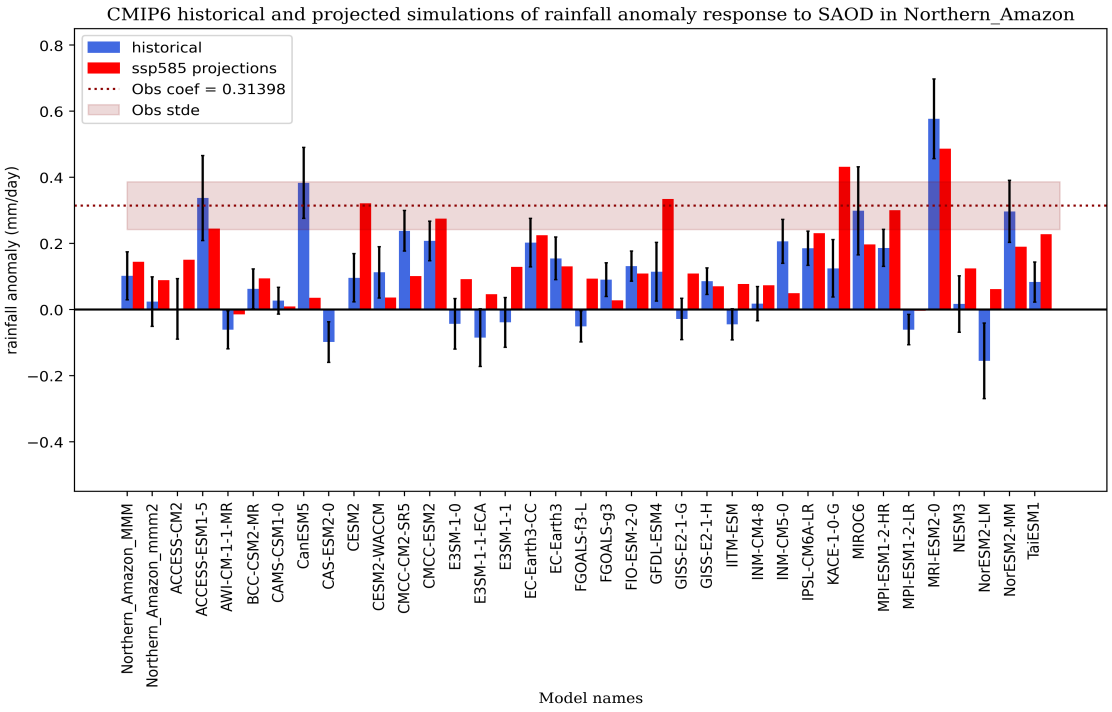

Figure 14: Regression of rainfall anomalies on normalized SAOD for Northern Amazon showing historical (blue bars) and projected (red bars) simulations. Observations is represented as the dotted horizontal line. Obs stde = Standard error of observations. The black error bars indicate the model standard error.

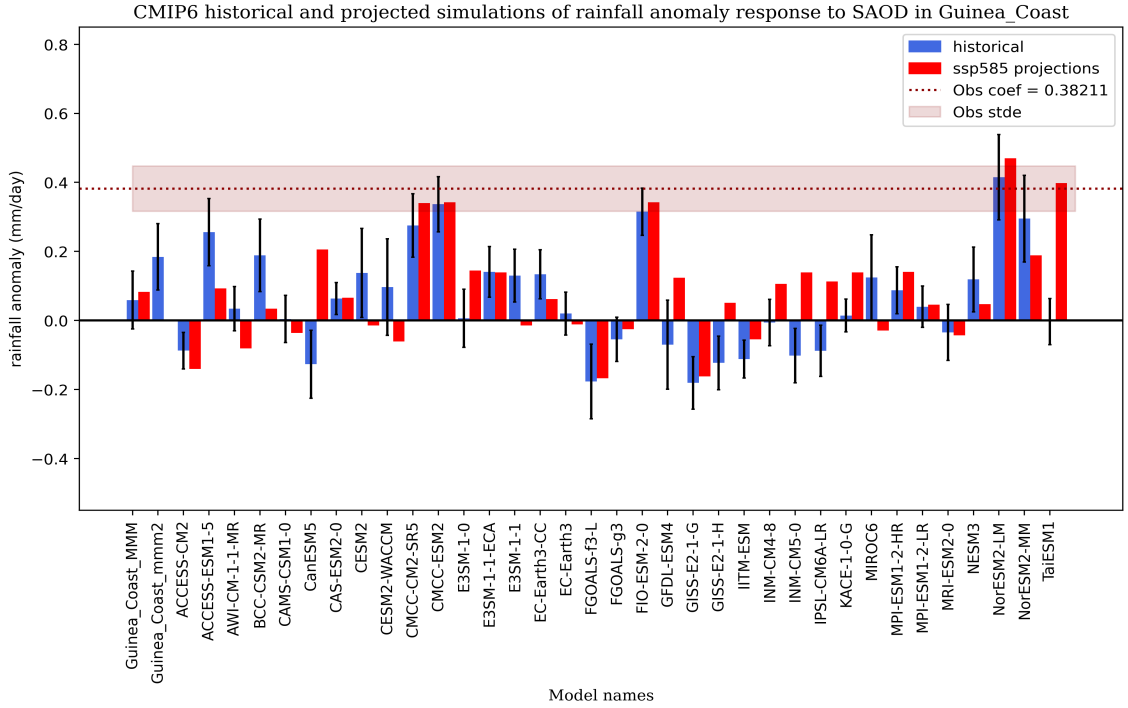

Figure 15: Regression of rainfall anomalies on normalized SAOD for Guinea Coast showing historical (blue bars) and projected (red bars) simulations. Observations is represented as the dotted horizontal line. Obs stde = Standard error of observations. The black error bars indicate the model standard error.

Central Africa

For Central Africa, the observed regression coefficient β = 0.19. Eight models' historical simulations are closest to observation; CESM2, FIO-ESM-2-0, KACE-1-0-G, E3SM-1-1, INM-CM4-8, CMCC-CM2-SR5, MIROC6, and MPI-ESMI-2-HR. The first four in this list have projections that indicate reduced rainfall response to SAOD in the future. On the other hand, two of the models (INM-CM4-8 and CMCC-CM2-SR5) have future simulations that show an increase in rainfall anomaly response to SAOD, while the last two on the list have projected simulations that show an opposite sign (negative coefficients). Notably, the two multi-model means (mmm and mmm2) also have historical simulations close to the observation, with both showing future decrease in rainfall anomaly response to SAOD (Fig. 16). 15 models' historical simulations overestimate the observed rainfall response to SAOD. They include CESM2, FIO-ESM-2-0, KACE-1-0-G, CMCC-CM2-SR5, E3SM-1-1, EC-Earth3, E3SM-1-0, BCC-CSM2-MR, CMCC-ESM2, E3SM-1-1-ECA, ACCESS-CM2, NorESM2-MM, FGOALS-g3, EC-Earth3-CC, ACCESS-ESM1-5 (Fig. 16). For most of these models, however, their projected simulations indicate a decrease in rainfall response to SAOD – notably CMCC-ESM2, ESM-1-1, EC-Earth3 have projections almost equal to the observed value. Only four models (GISS-E2-1-G, GFDL-ESM4, GISS-E2-1-H, CanESM5) indicate a negative-sign coefficient in their historical simulations while there are six projection simulations with the negative sign (AWI-CM-1-1-MR, GISS-E2-1-G, GISS-E2-1-H, MIROC6, MPI-ESM1-2-HR, and NESM3).

South East Brazil

SAOD has an observed inverse influence on rainfall anomaly in this region (β = -0.12) (Fig. 17). Most of the models' historical simulations significantly underestimate this observed inverse SAOD-rainfall relationship. Moreover, 14 models (CanESM5, E3SM-1-1-ECA, INM-CM4-8, E3SM-1-1, MPI-ESM1-2-HR, IPSL-CM6A-LR, GISS-E2-1-H, EC-Earth3, FGOALS-f3-L, CAS-ESM2-0, KACE-1-0-G, TaiESM1, GISS-E2-1-G, and IITM-ESM) have historic simulations with an opposite sign to observations. Two models' historic simulations are closest to observation namely ACCESS-CM2 and ACCESS-ESM1-5. While the former overestimates its historical simulation, with its projection indicating a reduction in the rainfall response to SAOD, the latter underestimates its historic simulation and has a projection with a positive sign in contrast to observations (Fig. 17). The projected simulations show a spread in model behaviour. Some model projections are very close to observations

(MPI-ESM1-2-HR, EC-Earth3-CC), while other models (NESM3, ACCESS-ESM1-5, IPSL-CM6A-LR, FIO-ESM-2-0, NorESM2-0, KACE-1-0-G, MPI-ESM1-2-LR, E3SM-1-1, INM-CM5-0, TaiESM1, CAS-ESM2-0, FGOALS-f3-L, GISS-E2-1-H, NorESM2-MM, CESM2-WACCM, GISS-E2-1-G, CESM2, MIROC6, IITM-ESM), and the two multi-model means (mmm and mmm2) have positive sign coefficients in the future (Fig. 17). Generally speaking, models' performance is poorest in this region.

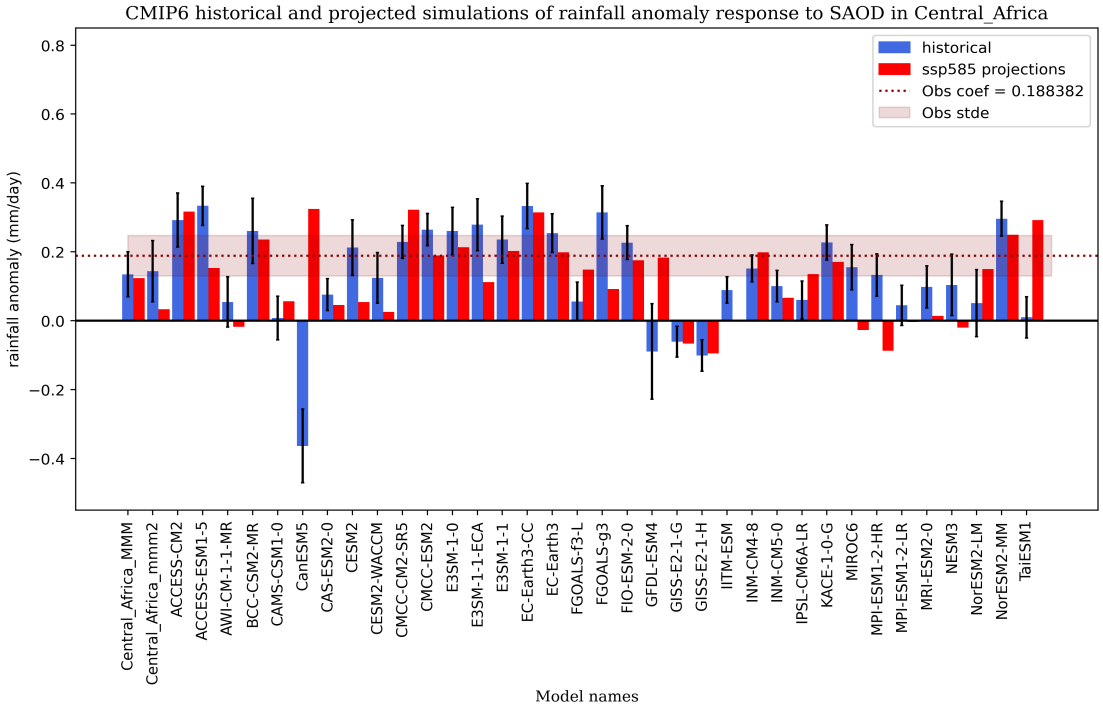

Figure 16: Regression of rainfall anomalies on normalized SAOD for Central Africa showing historical (blue bars) and projected (red bars) simulations. Observations is represented as the dotted horizontal line. Obs stde = Standard error of observations. The black error bars indicate the model standard error.

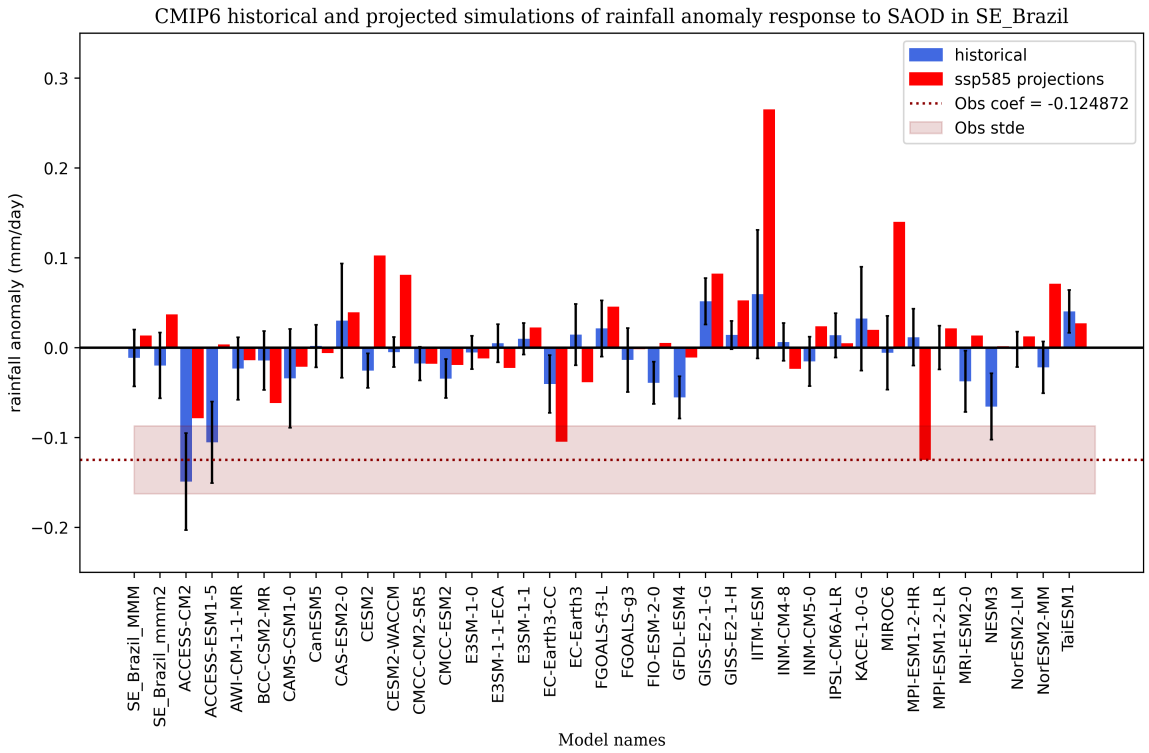

Figure 17: Regression of rainfall anomalies on normalized SAOD for South East Brazil showing historical (blue bars) and projected (red bars) simulations. Observations is represented as the dotted horizontal line. Obs stde = Standard error of observations. The black error bars indicate the model standard error.

4.2.3 A weakening of the SAOD impacts on regional rainfall under SSP585

Here we grouped the CMIP6 ensemble according to their performance, relative to observations, in simulating the historical SAODI–rainfall relationship in each region. Three categories were defined;

- Category 1: Models with the same sign of correlation as observations and also statistically significant ($p < 0.05$). The Category 1 models are considered the best performing and most realistic models in simulating the SAOD–rainfall relationship in a region.

- Category 2: Models with same sign of correlation as observations but not statistically significant. These models are in the intermediate performance category.

- Category 3: Models with an opposite sign of correlation from observations, representing the worst performing models for the respective regions.

First, we categorized the models using the historical ensemble. Second, we used the models in each category to construct the ensemble mean in historical simulation. Finally, we matched this historical ensemble mean with the SSP585 ensemble mean for each region. In what follows, we present an assessment of the projections of the SAOD-regional rainfall in the

realistic models (that is, Category 1 models). The unrealistic models (Categories 2 and 3) are shown in the Appendix section for reference[5].

Focusing on Category 1, Central Africa had 23 models (52%) in Category 1, the highest among the regions, including E3SM-1-1, CMCC-CM2-HR4, E3SM-1-1-ECA, BCC-CSM2-MR, ACCESS-CM2, E3SM-1-0, EC-Earth3-AerChem, CESM2, INM-CM4-8, FGOALS-g3, MIROC6, IITM-ESM, INM-CM5- 0, MPI-ESM1-2-HR, KACE-1-0-G, EC-Earth3, FIO-ESM-2-0, CMCC-CM2-SR5, EC-Earth3-CC, CMCC-ESM2, SAM0-UNICON, ACCESS-ESM1-5, and NorESM2-MM. This was followed by the Northern Amazon which had 15 models (34%) (MRI-ESM2-0, CMCC-CM2-SR5, IPSL-CM6A-LR, CanESM5, CMCC-ESM2, MPI-ESM1-2-HR, NorESM2-MM, INM-CM5-0, NorCPM1, FIO-ESM-2-0, EC-Earth3-CC, ACCESS-ESM1-5, EC-Earth3, MIROC6, and GISS-E2-1-H) and then Guinea Coast with seven models (16%) (FIO-ESM-2-0, CMCC-ESM2, NorESM2-LM, CMCC-CM2-SR5, ACCESS-ESM1-5, SAM0-UNICON, and NorESM2-MM). On the other hand, South East Brazil exhibited the overall worst performance with only three models (7%) in Category 1 (ACCESS-CM2, GFDL-ESM4, ACCESS-ESM1-5). Notably, only one model (ACCESS-ESM1-5) performs well in all regions, while three models (CMCC-CM2-SR5, CMCC-ESM2, NorESM-MM) perform well in three of the regions with the exception of South East Brazil.

Figure 18 shows the ensemble mean of the historical and SSP585 projected simulations of Category 1 (best performing) models (Cat1EnsMean) in each region. For Northern Amazon, the Cat1EnsMean for the historical period (0.25 mm/day) underestimates the rainfall response to SAOD when compared with observations (0.31 mm/day). For Central Africa, historical Cat1EnsMean simulates a stronger influence of SAOD on rainfall anomaly (0.22 mm/day) when compared to observations (0.188 mm/day), while the historical Cat1EnsMean of Guinea Coast (0.32 mm/day) and South East Brazil (-0.10 mm/day) is lower than the observed rainfall response to SAOD (0.38 mm/day [Obs] and -0.12 mm/day [Obs], respectively). Notably, only the historical simulation for Guinea Coast falls outside the 95% confidence level when compared to observations, suggesting a statistically significant underestimation. The SSP585 Cat1EnsMean's indicate a decrease of SAOD influence on rainfall anomaly in all the regions - Northern Amazon (0.19 mm/day), Central Africa (0.15 mm/day), Guinea Coast (0.29 mm/day), and South East Brazil (-0.03 mm/day) – when

5 See ensemble mean of Category 2 & 3 with full list of models in each category in Appendix – figs. A4, A5 and Table 2.

compared to their respective observations and historical simulations. This decrease is statistically significant (compared to Observations) in all the regions except in Central Africa (Fig. 18). The future scenario considered in this study (SSP585) connotes high GHG forcing. Hence the best performing models in each region show a future where increase in GHG forcing would result in a weakening of SAOD influence on rainfall over land areas adjacent to the South Atlantic region.

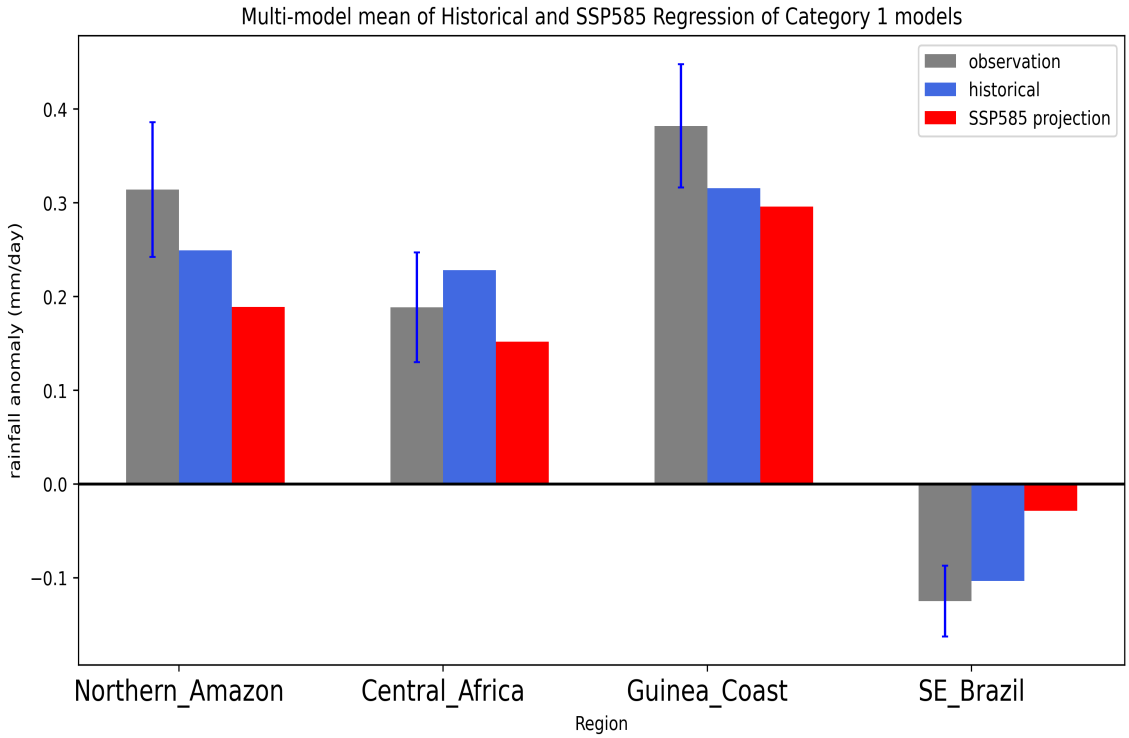

Figure 18: Ensemble mean of Category 1 models in each region. Blue error bars on Observations indicate the standard error for Observations at 95% confidence level. Historical and SSP585 bars that overlap with the error bars are not significantly different from Observations, while bars that fall beyond the error bars are significantly different from Observations.

5. Discussion

Our study evaluated the impact of SAOD on rainfall over adjacent continental areas in the South Atlantic region during the austral winter, and assessed the performance of CMIP6 models in representing this SAOD-rainfall relationship in the region. Correlation and regression analyses were performed between normalized SAODI and regional rainfall anomalies using data from observations and outputs from 44 CMIP6 models. We considered two scenarios – historical (1950 - 2014) and SSP585 projections (2015 – 2079) – in order to glean the model projections of future changes in the SAOD-rainfall relationship. Results from observations point to a strong statistically significant influence of SAOD on rainfall over four regions in Africa – Guinea Coast and Central Africa, and South America – Northern Amazon and South East Brazil – with Guinea Coast showing the strongest rainfall response to SAOD (β = 0.38 mm/day), while the weakest rainfall response was over South East Brazil (β = -0.12 mm/day). The correlation and regression analysis of individual models revealed a spread in model behavior across the regions. SAODI-rainfall regression analyses for the SSP585 future scenario using the ensemble of best performing models in each region indicated a reduction in rainfall response to SAOD influence across all the regions.

The observed SAODI-rainfall relationship here is consistent with previous studies that used different periods including Nana et al. (2023); based on 1981 - 2018, Nnamchi et al. (2013); based on 1950 - 2010, and Nnamchi & Li (2016); based on 1959 - 2009. Nnamchi et al. (2013) demonstrated the significant impact of SAOD on rainfall anomalies over the Guinea Coast, while Nana et al. (2023) identified statistically significant correlations between SAOD and rainfall in southwestern Central Africa, which coincides with the Central Africa domain defined in our study. During positive SAOD events, increased rainfall is associated with increased moisture convergence in the lower layers of the troposphere over the NEP which strengthens the upward motion occurring over the equatorial Atlantic region leading to the convergence of mass on a large scale that extends towards the coastal areas (Nana et al., 2023; Nnamchi et al., 2013).

Rainfall variability in the Amazon region is known to be primarily influenced by the ENSO (Espinoza et al., 2011; Latif & Keenlyside, 2009; Liebmann & Marengo, 2001), while SST anomalies in the tropical Atlantic also play a role (Baker et al., 2001; Marengo, 2004). The observed correlation between the SAOD and rainfall over the Northern Amazon during

austral winter in our study is r = 0.48 [Obs]. This translates to 23% explained variance, suggesting the roles of other influences including ENSO, which is not explicitly accounted for in our analysis.

Model simulations of the SAOD-rainfall correlation in our study reveals variations in model behavior across the different regions. While the model performance was generally acceptable for Central Africa and Northern Amazon (52% and 34% of models perform well, respectively), it was less satisfactory for the Guinea Coast (16%) and South East Brazil (7%), where more than 40% of the models simulated a correlation sign opposite to observations in both regions.

Previous research by Yang & Huang (2023) has suggested that CMIP6 models' ability to simulate better rainfall-SST correlations in the tropics depends on accurate representation of climatological precipitation in the region. Nonetheless, several studies evaluating CMIP6 model performance in various regions have pointed to deficiencies in simulating rainfall variability (Almazroui, 2020; Firpo et al., 2022; James et al., 2018; Yang et al., 2021). In Africa, this deficiency has been attributed to an erroneous southward shift of the ITCZ during the MAM season (James et al., 2018; Richter & Tokinaga, 2020), which could explain the generally poor performance of the CMIP6 models over the Guinea Coast in our study. While increasing spatial resolution has shown some improvement in rainfall simulations over West Africa (Ajibola et al., 2020), it has not led to a significant breakthrough (Exarchou et al., 2018; Richter & Tokinaga, 2020). Lyon (2022) even found that CMIP6 models' ability to represent rainfall in the Greater Horn of Africa depended more on the adequate simulation of climatological SST than spatial resolution.

CMIP6 models generally provide adequate simulations of SST variability in the tropical and subtropical Atlantic (Nnamchi et al., 2017; Richter & Tokinaga, 2020), despite persisting biases, notably the eastern tropical Atlantic warm bias (Exarchou et al., 2018; Richter & Tokinaga, 2020; Wang et al., 2022). Weber et al. (2023) studied the influence of the regional atmosphere–ocean coupling on simulated rainfall and its characteristics over Africa and showed that reduced SST warm biases in the eastern tropical Atlantic Ocean contributes to a more realistic simulation of rainfall over most coastal regions of West Africa and over southern Africa. Persistent SST biases in many CMIP6 models over the central equatorial and northern Pacific have been shown to impair their ability to simulate teleconnections between the Indo-Western Pacific Ocean Capacitor mode and the Indian summer monsoon (Darshana

et al., 2022), emphasizing the profound impact of SST biases on CMIP6 models' ability to simulate air-sea interactions.

In regions like the Guinea Coast and South East Brazil, the fact that many models exhibit erroneous representations of rainfall response to SAOD could be attributed to a variety of factors. Over the Guinea Coast, inadequate simulation of convective processes may be a major contributing factor. On the other hand, over South East Brazil, convective processes are not important during JJA as this is the dry season of the region. In this case, poor model performance could be attributed to a deficiency in simulating the frequency, intensity and trajectory of extratropical processes that are known to have substantial influence on rainfall variability in South East Brazil during JJA (Reboita et al., 2021). Further analyses and experiments are required to confirm these hypotheses. Nevertheless, our study shows a diverse behavior of CMIP6 models in representing the impacts of SAOD on regional rainfall variability, and it is recommended to improve the parametrization of local convective processes and extratropical factors influencing rainfall in these models (James et al., 2018; Richter & Tokinaga, 2020).

While the ensemble mean of all the models showed an increase in SAOD influence on rainfall under SSP585 in three of the four regions – Northern Amazon, Guinea Coast and South East Brazil (Fig 13(c)), the simulations of the best performing models in each region indicated a weakening of SAOD influence on rainfall variability in all regions under the high GHG emission. This weakening is statistically significant in all the regions except in Central Africa (see Fig. 18). Notably some of the best performing models in each region also simulate an increase in rainfall response to SAOD under SSP585 (see Figs. 14-17). This diversity in model behavior further highlights the deficiencies of CMIP6 models, but also suggests a change in rainfall patterns over the regions. This, in turn, can have substantial implications for the already stressed socio-ecological landscape in the considered regions, affecting agricultural practices (Hansen, 2005), water and energy resource management (Conway et al., 2017), and even health (Thomson et al., 2017). Although our study does not consider other projection scenarios (e.g., SSP126, SSP245, SSP370), lower emission trajectories have been shown to result in reduced future changes in rainfall patterns (Almazroui et al., 2021). Hence, our results underscore the importance of reducing GHG emissions to mitigate the impacts of climate change.

It is essential to acknowledge that this study is limited by its focus on the simulation of the SAOD-rainfall relationship over the adjacent continental areas and does not delve into the

causes of the observed deficiencies. Also, other oceanic modes of variability that influence rainfall, such as the ENSO, are not considered here in terms of their connection with the SAOD-rainfall relationship. Further research should therefore involve process analysis that would shed more light on the mechanisms underlying the varying individual model performances observed in each region, and the possible impacts of other modes of variability on the SAOD influence on rainfall, particularly in the SSP585 scenario.

6. Conclusion

The South Atlantic region experiences various modes of climate variability, which are shifts from the average conditions and occurring at different timescales. Among these modes, the SAOD stands out as the leading mode of variability with profound impacts on the climatic conditions of the region, particularly on rainfall patterns over the land areas (Bombardi et al., 2014b; Nana et al., 2023; Nnamchi et al., 2013). The land regions in the South Atlantic considered in this study are highly sensitive to rainfall fluctuations, as changes in rainfall can evidently affect the livelihoods of the local populations and critical ecosystems. Hence, it is crucial to use models that can accurately simulate and predict the interannual variations in rainfall for these regions. In light of the observed influence of SAOD on regional rainfall, our study evaluated the performance of CMIP6 models in capturing the significant interannual fluctuations between SAOD and rainfall during the austral winter in the South Atlantic region.

Analyses of SAOD-regional rainfall relationship in observations revealed that the SAOD has strong influence on rainfall over four regions; two in Africa – Guinea Coast and Central Africa, and two in South America – Northern Amazon and South East Brazil. The CMIP6 ensemble historical simulations of the SAOD-rainfall correlation was better in some regions (Central Africa and Northern Amazon) than in the others (Guinea Coast and Southeast Brazil). Correlation analysis of individual models showed a spread in performance across the regions. We then categorized the model performance into three groups: Category 1 represented the best-performing and realistic models, Category 2 included intermediate models, and Category 3 encompassed the least performing models with significant deviations from observations. Regression analyses for a future scenario with increasing greenhouse forcing showed mixed results: the multimodel ensemble mean indicated an increase of rainfall response to SAOD in three of the regions while the ensemble mean of the best performing models indicated a reduction in rainfall response to SAOD influence.

In conclusion, this study reaffirms the significant impact of SAOD on rainfall variability in adjacent land areas of the South Atlantic and emphasizes the need to enhance CMIP6 models' capability to simulate this relationship. Furthermore, our results suggest that if greenhouse gas emissions remain uncontrolled, future rainfall patterns could be altered with unpredictable consequences for the affected regions.

7. Recommendations

Based on the findings of this study, the following recommendations are proposed:

1. Conduct further studies focusing on the process analyses of each model to identify possible reasons for their varied performance relative to observations.

2. The SAOD has strong influence on rainfall in parts of Africa and South America and this connection demands more attention particularly with respect to improving the seasonal rainfall predictions in the regions.

3. Strengthen ongoing global efforts to mitigate greenhouse gas emissions and, especially in West and Central Africa, increase awareness and promote adaptation measures where changes in rainfall patterns have already resulted in catastrophic events such as extreme droughts and floods.

4. Carry out further investigations into the implications of the reduced rainfall response to SAOD and its impacts on seasonal rainfall predictability over the affected countries.

8. References

Ajibola, F. O., Zhou, B., Tchalim Gnitou, G., & Onyejuruwa, A. (2020). Evaluation of the Performance of CMIP6 HighResMIP on West African Precipitation. *Atmosphere*, *11*(10), 1053. https://doi.org/10.3390/atmos11101053

Alhamshry, A., Fenta, A. A., Yasuda, H., Kimura, R., & Shimizu, K. (2019). Seasonal Rainfall Variability in Ethiopia and Its Long-Term Link to Global Sea Surface Temperatures. *Water*, *12*(1), 55. https://doi.org/10.3390/w12010055

Almazroui, M. (2020). Changes in Temperature Trends and Extremes over Saudi Arabia for the Period 1978–2019. *Advances in Meteorology*, *2020*, 1–21. https://doi.org/10.1155/2020/8828421

Almazroui, M., Ashfaq, M., Islam, M. N., Rashid, I. U., Kamil, S., Abid, M. A., O'Brien, E., Ismail, M., Reboita, M. S., Sörensson, A. A., Arias, P. A., Alves, L. M., Tippett, M. K., Saeed, S., Haarsma, R., Doblas-Reyes, F. J., Saeed, F., Kucharski, F., Nadeem, I., … Sylla, M. B. (2021). Assessment of CMIP6 Performance and Projected Temperature and Precipitation Changes Over South America. *Earth Systems and Environment*, *5*(2), 155–183. https://doi.org/10.1007/s41748-021-00233-6

Baker, P. A., Seltzer, G. O., Fritz, S. C., Dunbar, R. B., Grove, M. J., Tapia, P. M., Cross, S. L., Rowe, H. D., & Broda, J. P. (2001). The History of South American Tropical Precipitation for the Past 25,000 Years. *Science*, *291*(5504), 640–643. https://doi.org/10.1126/science.291.5504.640

Bao, Y., Song, Z., & Qiao, F. (2020). FIO-ESM Version 2.0: Model Description and Evaluation. *Journal of Geophysical Research: Oceans*, *125*(6). https://doi.org/10.1029/2019JC016036

Bergquist, M., Nilsson, A., & Schultz, P. W. (2019). Experiencing a Severe Weather Event Increases Concern About Climate Change. *Frontiers in Psychology*, *10*, 220. https://doi.org/10.3389/fpsyg.2019.00220

Bi, D., Dix, M., Marsland, S., O'Farrell, S., Sullivan, A., Bodman, R., Law, R., Harman, I., Srbinovsky, J., Rashid, H. A., Dobrohotoff, P., Mackallah, C., Yan, H., Hirst, A., Savita, A., Dias, F. B., Woodhouse, M., Fiedler, R., & Heerdegen, A. (2020). Configuration and spin-up of ACCESS-CM2, the new generation Australian Community Climate and Earth System Simulator Coupled Model. *Journal of Southern Hemisphere Earth Systems Science*, *70*(1), 225–251. https://doi.org/10.1071/ES19040

Boko, M., Niang, I., Nyong, A., Vogel, A., Githeko, A., Medany, M., Osman-Elasha, B., Tabo, R., & Yanda, P. Z. (2007). *Africa climate change 2007: Impacts, adaptation and vulnerability: Contribution of working group II to the fourth assessment report of the intergovernmental panel on climate change*.

Bombardi, R. J., & Carvalho, L. M. (2011). The South Atlantic dipole and variations in the characteristics of the South American Monsoon in the WCRP-CMIP3 multi-model simulations. *Climate Dynamics*, *36*, 2091–2102.

Bombardi, R. J., Carvalho, L. M., & Jones, C. (2014a). Simulating the influence of the South Atlantic dipole on the South Atlantic convergence zone during neutral ENSO. *Theoretical and Applied Climatology*, *118*, 251–269.

Bombardi, R. J., Carvalho, L. M. V., Jones, C., & Reboita, M. S. (2014b). Precipitation over eastern South America and the South Atlantic Sea surface temperature during neutral ENSO periods. *Climate Dynamics*, *42*(5–6), 1553–1568. https://doi.org/10.1007/s00382-013-1832-7

Bonal, D., Burban, B., Stahl, C., Wagner, F., & Hérault, B. (2016). The response of tropical rainforests to drought—Lessons from recent research and future prospects. *Annals of Forest Science*, *73*(1), 27–44. https://doi.org/10.1007/s13595-015-0522-5

Boucher, O., Denvil, S., Levavasseur, G., Cozic, A., Caubel, A., Foujols, M.-A., Meurdesoif, Y., Vuichard, N., Ghattas, J., & Cadule, P. (2019). *IPSL IPSL-CM6A-LR model output prepared for CMIP6 LUMIP* (Version 20220607) [Application/x-netcdf]. Earth System Grid Federation. https://doi.org/10.22033/ESGF/CMIP6.1528

Brown, D., Brownrigg, R., Haley, M., & Huang, W. (2012). *NCAR Command Language (NCL)* [NCL supports the following data formats - NetCDF, HDF4, HDF5, HDF-EOS2, HDF-EOS5, GRIB1, GRIB2, shapefiles.]. UCAR/NCAR - Computational and Information Systems Laboratory (CISL). https://doi.org/10.5065/D6WD3XH5

Camberlin, P., Janicot, S., & Poccard, I. (2001). Seasonality and atmospheric dynamics of the teleconnection between African rainfall and tropical sea-surface temperature: Atlantic vs. ENSO. *International Journal of Climatology*, *21*(8), 973–1005. https://doi.org/10.1002/joc.673

Cao, J., Wang, B., Yang, Y.-M., Ma, L., Li, J., Sun, B., Bao, Y., He, J., Zhou, X., & Wu, L. (2018). The NUIST Earth System Model (NESM) version 3: Description and preliminary evaluation. *Geoscientific Model Development*, *11*(7), 2975–2993. https://doi.org/10.5194/gmd-11-2975-2018

Chai, Z. (2020). *CAS CAS-ESM2.0 model output prepared for CMIP6 CMIP* (Version 20230213) [Application/x-netcdf]. Earth System Grid Federation. https://doi.org/10.22033/ESGF/CMIP6.1944

Cherchi, A., Fogli, P. G., Lovato, T., Peano, D., Iovino, D., Gualdi, S., Masina, S., Scoccimarro, E., Materia, S., Bellucci, A., & Navarra, A. (2018). Global mean climate and main patterns of variability in the CMCC-CM2 coupled model. *Journal of Advances in Modeling Earth Systems*, 2018MS001369. https://doi.org/10.1029/2018MS001369

Conway, D., Dalin, C., Landman, W. A., & Osborn, T. J. (2017). Hydropower plans in eastern and southern Africa increase risk of concurrent climate-related electricity supply disruption. *Nature Energy*, *2*(12), 946–953.

Danabasoglu, G., Lamarque, J. -F., Bacmeister, J., Bailey, D. A., DuVivier, A. K., Edwards, J., Emmons, L. K., Fasullo, J., Garcia, R., Gettelman, A., Hannay, C., Holland, M. M., Large, W. G., Lauritzen, P. H., Lawrence, D. M., Lenaerts, J. T. M., Lindsay, K., Lipscomb, W. H., Mills, M. J., … Strand, W. G. (2020). The Community Earth System Model Version 2 (CESM2). *Journal of Advances in Modeling Earth Systems*, *12*(2). https://doi.org/10.1029/2019MS001916

Darshana, P., Chowdary, J. S., Parekh, A., & Gnanaseelan, C. (2022). Relationship between the Indo-western Pacific Ocean capacitor mode and Indian summer monsoon rainfall in CMIP6 models. *Climate Dynamics*, *59*(1–2), 393–415.

Döscher, R., Acosta, M., Alessandri, A., Anthoni, P., Arsouze, T., Bergman, T., Bernardello, R., Boussetta, S., Caron, L.-P., Carver, G., Castrillo, M., Catalano, F., Cvijanovic, I., Davini, P., Dekker, E., Doblas-Reyes, F. J., Docquier, D., Echevarria, P., Fladrich, U., … Zhang, Q. (2022). The EC-Earth3 Earth system model for the Coupled Model Intercomparison Project 6. *Geoscientific Model Development*, *15*(7), 2973–3020. https://doi.org/10.5194/gmd-15-2973-2022

Dunne, J. P., Horowitz, L. W., Adcroft, A. J., Ginoux, P., Held, I. M., John, J. G., Krasting, J. P., Malyshev, S., Naik, V., Paulot, F., Shevliakova, E., Stock, C. A., Zadeh, N., Balaji, V., Blanton, C., Dunne, K. A., Dupuis, C., Durachta, J., Dussin, R., … Zhao, M. (2020). The GFDL Earth System Model Version 4.1 (GFDL-ESM 4.1): Overall

Coupled Model Description and Simulation Characteristics. *Journal of Advances in Modeling Earth Systems*, *12*(11). https://doi.org/10.1029/2019MS002015

Ecuador Amazon Rainforest Weather and Month-to-Month Temperatures. (n.d.). Retrieved July 30, 2023, from https://galapagosinsiders.com/travel-blog/climate-weather-amazon-rainforest-temperatures/

Espinoza, J. C., Ronchail, J., Guyot, J. L., Junquas, C., Vauchel, P., Lavado, W., Drapeau, G., & Pombosa, R. (2011). Climate variability and extreme drought in the upper Solimões River (western Amazon Basin): Understanding the exceptional 2010 drought: DROUGHTS IN THE UPPER SOLIMÕES. *Geophysical Research Letters*, *38*(13), n/a-n/a. https://doi.org/10.1029/2011GL047862

Exarchou, E., Prodhomme, C., Brodeau, L., Guemas, V., & Doblas-Reyes, F. (2018). Origin of the warm eastern tropical Atlantic SST bias in a climate model. *Climate Dynamics*, *51*(5–6), 1819–1840. https://doi.org/10.1007/s00382-017-3984-3

Eyring, V., Bony, S., Meehl, G. A., Senior, C. A., Stevens, B., Stouffer, R. J., & Taylor, K. E. (2016). Overview of the Coupled Model Intercomparison Project Phase 6 (CMIP6) experimental design and organization. *Geoscientific Model Development*, *9*(5), 1937–1958. https://doi.org/10.5194/gmd-9-1937-2016

Firpo, M. Â. F., Guimarães, B. D. S., Dantas, L. G., Silva, M. G. B. D., Alves, L. M., Chadwick, R., Llopart, M. P., & Oliveira, G. S. D. (2022). Assessment of CMIP6 models' performance in simulating present-day climate in Brazil. *Frontiers in Climate*, *4*, 948499. https://doi.org/10.3389/fclim.2022.948499

Foley, J. A., Botta, A., Coe, M. T., & Costa, M. H. (2002). El Niño–Southern oscillation and the climate, ecosystems and rivers of Amazonia. *Global Biogeochemical Cycles*, *16*(4), 79–1.

Foltz, G. R., Brandt, P., Richter, I., Rodríguez-Fonseca, B., Hernandez, F., Dengler, M., Rodrigues, R. R., Schmidt, J. O., Yu, L., Lefevre, N., Da Cunha, L. C., McPhaden, M. J., Araujo, M., Karstensen, J., Hahn, J., Martín-Rey, M., Patricola, C. M., Poli, P., Zuidema, P., … Reul, N. (2019). The Tropical Atlantic Observing System. *Frontiers in Marine Science*, *6*, 206. https://doi.org/10.3389/fmars.2019.00206

Golaz, J., Caldwell, P. M., Van Roekel, L. P., Petersen, M. R., Tang, Q., Wolfe, J. D., Abeshu, G., Anantharaj, V., Asay-Davis, X. S., Bader, D. C., Baldwin, S. A., Bisht, G., Bogenschutz, P. A., Branstetter, M., Brunke, M. A., Brus, S. R., Burrows, S. M., Cameron-Smith, P. J., Donahue, A. S., … Zhu, Q. (2019). The DOE E3SM Coupled Model Version 1: Overview and Evaluation at Standard Resolution. *Journal of Advances in Modeling Earth Systems*, *11*(7), 2089–2129. https://doi.org/10.1029/2018MS001603

Gulev, S. K., Thorne, P. W., Ahn, J., Dentener, F. J., Domingues, C. M., Gerland, S., Gong, D., Kaufman, D. S., Nnamchi, H. C., & Quaas, J. (2021). *Changing state of the climate system*.

Guo, C., Bentsen, M., Bethke, I., Ilicak, M., Tjiputra, J., Toniazzo, T., Schwinger, J., & Otterå, O. H. (2019). Description and evaluation of NorESM1-F: A fast version of the Norwegian Earth System Model (NorESM). *Geoscientific Model Development*, *12*(1), 343–362. https://doi.org/10.5194/gmd-12-343-2019

Haarsma, R. J., Campos, E. J., & Molteni, F. (2003). Atmospheric response to South Atlantic SST dipole. *Geophysical Research Letters*, *30*(16).

Hansen, J. W. (2005). Integrating seasonal climate prediction and agricultural models for insights into agricultural practice. *Philosophical Transactions of the Royal Society B: Biological Sciences*, *360*(1463), 2037–2047.

He, B., Yu, Y., Bao, Q., Lin, P., Liu, H., Li, J., Wang, L., Liu, Y., Wu, G., Chen, K., Guo, Y., Zhao, S., Zhang, X., Song, M., & Xie, J. (2020). CAS FGOALS-f3-L model dataset

descriptions for CMIP6 DECK experiments. *Atmospheric and Oceanic Science Letters*, *13*(6), 582–588. https://doi.org/10.1080/16742834.2020.1778419

Imbol Koungue, R. A., Brandt, P., Lübbecke, J., Prigent, A., Martins, M. S., & Rodrigues, R. R. (2021). The 2019 Benguela Niño. *Frontiers in Marine Science*, *8*, 800103. https://doi.org/10.3389/fmars.2021.800103

James, R., Washington, R., Abiodun, B., Kay, G., Mutemi, J., Pokam, W., Hart, N., Artan, G., & Senior, C. (2018). Evaluating Climate Models with an African Lens. *Bulletin of the American Meteorological Society*, *99*(2), 313–336. https://doi.org/10.1175/BAMS-D-16-0090.1

Keenlyside, N. S., & Latif, M. (2007). Understanding Equatorial Atlantic Interannual Variability. *Journal of Climate*, *20*(1), 131–142. https://doi.org/10.1175/JCLI3992.1

Kelley, M., Schmidt, G. A., Nazarenko, L. S., Bauer, S. E., Ruedy, R., Russell, G. L., Ackerman, A. S., Aleinov, I., Bauer, M., Bleck, R., Canuto, V., Cesana, G., Cheng, Y., Clune, T. L., Cook, B. I., Cruz, C. A., Del Genio, A. D., Elsaesser, G. S., Faluvegi, G., … Yao, M. (2020). GISS-E2.1: Configurations and Climatology. *Journal of Advances in Modeling Earth Systems*, *12*(8). https://doi.org/10.1029/2019MS002025

Latif, M., & Keenlyside, N. S. (2009). El Niño/Southern Oscillation response to global warming. *Proceedings of the National Academy of Sciences*, *106*(49), 20578–20583. https://doi.org/10.1073/pnas.0710860105

Lee, J., Kim, J., Sun, M.-A., Kim, B.-H., Moon, H., Sung, H. M., Kim, J., & Byun, Y.-H. (2020). Evaluation of the Korea Meteorological Administration Advanced Community Earth-System model (K-ACE). *Asia-Pacific Journal of Atmospheric Sciences*, *56*(3), 381–395. https://doi.org/10.1007/s13143-019-00144-7

Lee, W.-L., & Liang, H.-C. (2020). *AS-RCEC TaiESM1.0 model output prepared for CMIP6 ScenarioMIP* (Version 20230220) [Application/x-netcdf]. Earth System Grid Federation. https://doi.org/10.22033/ESGF/CMIP6.9688

Liebmann, B., & Marengo, JoséA. (2001). Interannual Variability of the Rainy Season and Rainfall in the Brazilian Amazon Basin. *Journal of Climate*, *14*(22), 4308–4318. https://doi.org/10.1175/1520-0442(2001)014<4308:IVOTRS>2.0.CO;2

Lübbecke, J. F., Böning, C. W., Keenlyside, N. S., & Xie, S.-P. (2010). On the connection between Benguela and equatorial Atlantic Niños and the role of the South Atlantic Anticyclone. *Journal of Geophysical Research*, *115*(C9), C09015. https://doi.org/10.1029/2009JC005964

Lyon, B. (2022). Biases in sea surface temperature and the annual cycle of Greater Horn of Africa rainfall in CMIP6. *International Journal of Climatology*, *42*(8), 4179–4186.

Marengo, J. A. (2004). Interdecadal variability and trends of rainfall across the Amazon basin. *Theoretical and Applied Climatology*, *78*(1–3). https://doi.org/10.1007/s00704-004-0045-8

Mauritsen, T., Bader, J., Becker, T., Behrens, J., Bittner, M., Brokopf, R., Brovkin, V., Claussen, M., Crueger, T., Esch, M., Fast, I., Fiedler, S., Fläschner, D., Gayler, V., Giorgetta, M., Goll, D. S., Haak, H., Hagemann, S., Hedemann, C., … Roeckner, E. (2019). Developments in the MPI-M Earth System Model version 1.2 (MPI-ESM1.2) and Its Response to Increasing CO_2. *Journal of Advances in Modeling Earth Systems*, *11*(4), 998–1038. https://doi.org/10.1029/2018MS001400

Mizuta, R., Yoshimura, H., Murakami, H., Matsueda, M., Endo, H., Ose, T., Kamiguchi, K., Hosaka, M., Sugi, M., Yukimoto, S., Kusunoki, S., & Kitoh, A. (2012). Climate Simulations Using MRI-AGCM3.2 with 20-km Grid. *Journal of the Meteorological Society of Japan. Ser. II*, *90A*(0), 233–258. https://doi.org/10.2151/jmsj.2012-A12

Morioka, Y., Masson, S., Terray, P., Prodhomme, C., Behera, S. K., & Masumoto, Y. (2014). Role of Tropical SST Variability on the Formation of Subtropical Dipoles. *Journal of Climate*, *27*(12), 4486–4507. https://doi.org/10.1175/JCLI-D-13-00506.1

Morioka, Y., Tozuka, T., & Yamagata, T. (2011). On the Growth and Decay of the Subtropical Dipole Mode in the South Atlantic. *Journal of Climate*, *24*(21), 5538–5554. https://doi.org/10.1175/2011JCLI4010.1

Moura, A. D., & Shukla, J. (1981). On the dynamics of droughts in northeast Brazil: Observations, theory and numerical experiments with a general circulation model. *Journal of the Atmospheric Sciences*, *38*(12), 2653–2675.

Müller, W. A., Jungclaus, J. H., Mauritsen, T., Baehr, J., Bittner, M., Budich, R., Bunzel, F., Esch, M., Ghosh, R., Haak, H., Ilyina, T., Kleine, T., Kornblueh, L., Li, H., Modali, K., Notz, D., Pohlmann, H., Roeckner, E., Stemmler, I., … Marotzke, J. (2018). A Higher-resolution Version of the Max Planck Institute Earth System Model (MPI-ESM1.2-HR). *Journal of Advances in Modeling Earth Systems*, *10*(7), 1383–1413. https://doi.org/10.1029/2017MS001217

Muller-Karger, E., Piola, A., Verheye, H., O'Brien, T., & Lorenzoni. (2017). *South Atlantic Ocean* (pp. 83–96).

Nana, H. N., Tanessong, R. S., Tchotchou, L. A. D., Tamoffo, A. T., Moihamette, F., & Vondou, D. A. (2023). Influence of strong South Atlantic Ocean Dipole on the Central African rainfall's system. *Climate Dynamics*. https://doi.org/10.1007/s00382-023-06892-7

Neubauer, D., Ferrachat, S., Siegenthaler-Le Drian, C., Stier, P., Partridge, D. G., Tegen, I., Bey, I., Stanelle, T., Kokkola, H., & Lohmann, U. (2019). The global aerosol–climate model ECHAM6.3–HAM2.3 – Part 2: Cloud evaluation, aerosol radiative forcing, and climate sensitivity. *Geoscientific Model Development*, *12*(8), 3609–3639. https://doi.org/10.5194/gmd-12-3609-2019

Nnamchi, H. C., Kucharski, F., Keenlyside, N. S., & Farneti, R. (2017). Analogous seasonal evolution of the South Atlantic SST dipole indices: South Atlantic SST dipole indices. *Atmospheric Science Letters*, *18*(10), 396–402. https://doi.org/10.1002/asl.781

Nnamchi, H. C., Latif, M., Keenlyside, N. S., Kjellsson, J., & Richter, I. (2021). Diabatic heating governs the seasonality of the Atlantic Niño. *Nature Communications*, *12*(1), 376. https://doi.org/10.1038/s41467-020-20452-1

Nnamchi, H. C., & Li, J. (2011). Influence of the South Atlantic Ocean Dipole on West African Summer Precipitation. *Journal of Climate*, *24*(4), 1184–1197. https://doi.org/10.1175/2010JCLI3668.1

Nnamchi, H. C., & Li, J. (2016). Floods and droughts along the Guinea Coast in connection with the South Atlantic Dipole. In J. Li, R. Swinbank, R. Grotjahn, & H. Volkert (Eds.), *Dynamics and Predictability of Large-Scale, High-Impact Weather and Climate Events* (1st ed., pp. 271–279). Cambridge University Press. https://doi.org/10.1017/CBO9781107775541.023

Nnamchi, H. C., Li, J., & Anyadike, R. N. C. (2011). Does a dipole mode really exist in the South Atlantic Ocean? *Journal of Geophysical Research*, *116*(D15), D15104. https://doi.org/10.1029/2010JD015579

Nnamchi, H. C., Li, J., Kang, I.-S., & Kucharski, F. (2013). Simulated impacts of the South Atlantic Ocean Dipole on summer precipitation at the Guinea Coast. *Climate Dynamics*, *41*(3–4), 677–694. https://doi.org/10.1007/s00382-012-1629-0

Nnamchi, H. C., Li, J., Kucharski, F., Kang, I.-S., Keenlyside, N. S., Chang, P., & Farneti, R. (2016). An Equatorial–Extratropical Dipole Structure of the Atlantic Niño. *Journal of Climate*, *29*(20), 7295–7311. https://doi.org/10.1175/JCLI-D-15-0894.1

Okumura, Y., & Xie, S.-P. (2004). Interaction of the Atlantic Equatorial Cold Tongue and the African Monsoon*. *Journal of Climate*, *17*(18), 3589–3602. https://doi.org/10.1175/1520-0442(2004)017<3589:IOTAEC>2.0.CO;2

Park, S., & Shin, J. (2019). *SNU SAM0-UNICON model output prepared for CMIP6 CMIP* (Version 20221012) [Application/x-netcdf]. Earth System Grid Federation. https://doi.org/10.22033/ESGF/CMIP6.1489

Pezzi, L. P., Quadro, M. F. L., Lorenzzetti, J. A., Miller, A. J., Rosa, E. B., Lima, L. N., & Sutil, U. A. (2022). The effect of Oceanic South Atlantic Convergence Zone episodes on regional SST anomalies: The roles of heat fluxes and upper-ocean dynamics. *Climate Dynamics*, *59*(7–8), 2041–2065. https://doi.org/10.1007/s00382-022-06195-3

Pielke, R. A., Cotton, W., Walko, R. e a1, Tremback, C., Lyons, W. A., Grasso, L., Nicholls, M., Moran, M., Wesley, D., & Lee, T. (1992). A comprehensive meteorological modeling system—RAMS. *Meteorology and Atmospheric Physics*, *49*, 69–91.

Polo, I., Rodríguez-Fonseca, B., Losada, T., & García-Serrano, J. (2008). Tropical Atlantic Variability Modes (1979–2002). Part I: Time-Evolving SST Modes Related to West African Rainfall. *Journal of Climate*, *21*(24), 6457–6475. https://doi.org/10.1175/2008JCLI2607.1

Raj, J., Bangalath, H. K., & Stenchikov, G. (2019). West African Monsoon: Current state and future projections in a high-resolution AGCM. *Climate Dynamics*, *52*(11), 6441–6461. https://doi.org/10.1007/s00382-018-4522-7

Rayner, N. A. (2003). Global analyses of sea surface temperature, sea ice, and night marine air temperature since the late nineteenth century. *Journal of Geophysical Research*, *108*(D14), 4407. https://doi.org/10.1029/2002JD002670

Rayner, N. A., Brohan, P., Parker, D. E., Folland, C. K., Kennedy, J. J., Vanicek, M., Ansell, T. J., & Tett, S. F. B. (2006). Improved Analyses of Changes and Uncertainties in Sea Surface Temperature Measured In Situ since the Mid-Nineteenth Century: The HadSST2 Dataset. *Journal of Climate*, *19*(3), 446–469. https://doi.org/10.1175/JCLI3637.1

Reboita, M., Reale, M., Rocha, R., Filippo, ·, Giuliani, ·, Coppola, E., Beatriz, ·, Luna-Niño, R., Llopart, M., Jose, ·, Torres, A., & Cavazos, T. (2021). Future changes in the wintertime cyclonic activity over the CORDEX-CORE southern hemisphere domains in a multi-model approach. *Climate Dynamics*, *57*, 3. https://doi.org/10.1007/s00382-020-05317-z

Riahi, K., Van Vuuren, D. P., Kriegler, E., Edmonds, J., O'Neill, B. C., Fujimori, S., Bauer, N., Calvin, K., Dellink, R., Fricko, O., Lutz, W., Popp, A., Cuaresma, J. C., Kc, S., Leimbach, M., Jiang, L., Kram, T., Rao, S., Emmerling, J., … Tavoni, M. (2017). The Shared Socioeconomic Pathways and their energy, land use, and greenhouse gas emissions implications: An overview. *Global Environmental Change*, *42*, 153–168. https://doi.org/10.1016/j.gloenvcha.2016.05.009

Richter, I., Behera, S. K., Masumoto, Y., Taguchi, B., Komori, N., & Yamagata, T. (2010). On the triggering of Benguela Niños: Remote equatorial versus local influences: TRIGGERING OF BENGUELA NIÑOS. *Geophysical Research Letters*, *37*(20), n/a-n/a. https://doi.org/10.1029/2010GL044461

Richter, I., & Tokinaga, H. (2020). An overview of the performance of CMIP6 models in the tropical Atlantic: Mean state, variability, and remote impacts. *Climate Dynamics*, *55*(9–10), 2579–2601. https://doi.org/10.1007/s00382-020-05409-w

Ritchie, H., Roser, M., & Rosado, P. (2020). CO_2 and greenhouse gas emissions. *Our World in Data*.

Robertson, A. W., Farrara, J. D., & Mechoso, C. R. (2003). Simulations of the atmospheric response to South Atlantic sea surface temperature anomalies. *Journal of Climate*, *16*(15), 2540–2551.

Robertson, A. W., & Mechoso, C. R. (2000). Interannual and interdecadal variability of the South Atlantic convergence zone. *Monthly Weather Review*, *128*(8), 2947–2957.

Ronchail, J., Cochonneau, G., Molinier, M., Guyot, J., De Miranda Chaves, A. G., Guimarães, V., & De Oliveira, E. (2002). Interannual rainfall variability in the Amazon basin and sea-surface temperatures in the equatorial Pacific and the tropical Atlantic Oceans. *International Journal of Climatology: A Journal of the Royal Meteorological Society*, *22*(13), 1663–1686.

Rong, X., Li, J., Chen, H., Xin, Y., Su, J., Hua, L., Zhou, T., Qi, Y., Zhang, Z., Zhang, G., & Li, J. (2018). The CAMS Climate System Model and a Basic Evaluation of Its Climatology and Climate Variability Simulation. *Journal of Meteorological Research*, *32*(6), 839–861. https://doi.org/10.1007/s13351-018-8058-x

Santis, W., Castellanos, P., & Campos, E. (2020). Memory Effect of the Southern Atlantic Subtropical Dipole. *Journal of Climate*, *33*(17), 7679–7696. https://doi.org/10.1175/JCLI-D-19-0745.1

Schlosser, C., Klar, J. K., Wake, B. D., Snow, J. T., Honey, D. J., Woodward, E. M. S., Lohan, M. C., Achterberg, E. P., & Moore, C. M. (2014). Seasonal ITCZ migration dynamically controls the location of the (sub)tropical Atlantic biogeochemical divide. *Proceedings of the National Academy of Sciences*, *111*(4), 1438–1442. https://doi.org/10.1073/pnas.1318670111

Schneider, U., Hänsel, S., Finger, P., Rustemeier, E., & Ziese, M. (2022). *GPCC Full Data Monthly Version 2022 at 1.0°: Monthly Land-Surface Precipitation from Rain-Gauges built on GTS-based and Historic Data: Globally Gridded Monthly Totals* (Version 2022, p. min. 20 MB-max. 300 MB per gzip archive (10 years per archive)) [NetCDF]. Global Precipitation Climatology Centre (GPCC) at Deutscher Wetterdienst. https://doi.org/10.5676/DWD_GPCC/FD_M_V2022_100

Scoccimarro, E., Bellucci, A., & Peano, D. (2020). *CMCC CMCC-CM2-HR4 model output prepared for CMIP6 CMIP* (Version 20220628) [Application/x-netcdf]. Earth System Grid Federation. https://doi.org/10.22033/ESGF/CMIP6.1358

Seland, Ø., Bentsen, M., Olivié, D., Toniazzo, T., Gjermundsen, A., Graff, L. S., Debernard, J. B., Gupta, A. K., He, Y.-C., Kirkevåg, A., Schwinger, J., Tjiputra, J., Aas, K. S., Bethke, I., Fan, Y., Griesfeller, J., Grini, A., Guo, C., Ilicak, M., … Schulz, M. (2020). Overview of the Norwegian Earth System Model (NorESM2) and key climate response of CMIP6 DECK, historical, and scenario simulations. *Geoscientific Model Development*, *13*(12), 6165–6200. https://doi.org/10.5194/gmd-13-6165-2020

Semmler, T., Danilov, S., Gierz, P., Goessling, H. F., Hegewald, J., Hinrichs, C., Koldunov, N., Khosravi, N., Mu, L., Rackow, T., Sein, D. V., Sidorenko, D., Wang, Q., & Jung, T. (2020). Simulations for CMIP6 With the AWI Climate Model AWI-CM-1-1. *Journal of Advances in Modeling Earth Systems*, *12*(9). https://doi.org/10.1029/2019MS002009

Sidorenko, D., Rackow, T., Jung, T., Semmler, T., Barbi, D., Danilov, S., Dethloff, K., Dorn, W., Fieg, K., Goessling, H. F., Handorf, D., Harig, S., Hiller, W., Juricke, S., Losch, M., Schröter, J., Sein, D. V., & Wang, Q. (2015). Towards multi-resolution global climate modeling with ECHAM6–FESOM. Part I: Model formulation and mean climate. *Climate Dynamics*, *44*(3–4), 757–780. https://doi.org/10.1007/s00382-014-2290-6

Sterl, A., & Hazeleger, W. (2003). Coupled variability and air-sea interaction in the South Atlantic Ocean. *Climate Dynamics*, *21*(7–8), 559–571. https://doi.org/10.1007/s00382-003-0348-y

Sultan, B., & Gaetani, M. (2016). Agriculture in West Africa in the Twenty-First Century: Climate Change and Impacts Scenarios, and Potential for Adaptation. *Frontiers in Plant Science*, *7*. https://www.frontiersin.org/articles/10.3389/fpls.2016.01262

Sultan, B., & Janicot, S. (2003). The West African Monsoon Dynamics. Part II: The "Preonset" and "Onset" of the Summer Monsoon. *Journal of Climate*, *16*(21), 3407–3427. https://doi.org/10.1175/1520-0442(2003)016<3407:TWAMDP>2.0.CO;2

Swapna, P., Krishnan, R., Sandeep, N., Prajeesh, A. G., Ayantika, D. C., Manmeet, S., & Vellore, R. (2018). Long-Term Climate Simulations Using the IITM Earth System Model (IITM-ESMv2) With Focus on the South Asian Monsoon. *Journal of Advances in Modeling Earth Systems*, *10*(5), 1127–1149. https://doi.org/10.1029/2017MS001262

Swart, N. C., Cole, J. N. S., Kharin, V. V., Lazare, M., Scinocca, J. F., Gillett, N. P., Anstey, J., Arora, V., Christian, J. R., Hanna, S., Jiao, Y., Lee, W. G., Majaess, F., Saenko, O. A., Seiler, C., Seinen, C., Shao, A., Sigmond, M., Solheim, L., … Winter, B. (2019). The Canadian Earth System Model version 5 (CanESM5.0.3). *Geoscientific Model Development*, *12*(11), 4823–4873. https://doi.org/10.5194/gmd-12-4823-2019

T., D., R., S., K., D., M., S., T., K., A., B., P., K., & R., W. (2002). Review of simulations of climate variability and change with the GFDL R30 coupled climate model. *Climate Dynamics*, *19*(7), 555–574. https://doi.org/10.1007/s00382-002-0249-5

Tatebe, H., Ogura, T., Nitta, T., Komuro, Y., Ogochi, K., Takemura, T., Sudo, K., Sekiguchi, M., Abe, M., Saito, F., Chikira, M., Watanabe, S., Mori, M., Hirota, N., Kawatani, Y., Mochizuki, T., Yoshimura, K., Takata, K., O'ishi, R., … Kimoto, M. (2019). Description and basic evaluation of simulated mean state, internal variability, and climate sensitivity in MIROC6. *Geoscientific Model Development*, *12*(7), 2727–2765. https://doi.org/10.5194/gmd-12-2727-2019

Thomson, M. C., Ukawuba, I., Hershey, C. L., Bennett, A., Ceccato, P., Lyon, B., & Dinku, T. (2017). Using rainfall and temperature data in the evaluation of national malaria control programs in Africa. *The American Journal of Tropical Medicine and Hygiene*, *97*(3 Suppl), 32.

Trzaska, S., Robertson, A. W., Farrara, J. D., & Mechoso, C. R. (2007). South Atlantic Variability Arising from Air–Sea Coupling: Local Mechanisms and Tropical–Subtropical Interactions. *Journal of Climate*, *20*(14), 3345–3365. https://doi.org/10.1175/JCLI4114.1

USAID. (2018). *Climate Risk Profile: West Africa*. United States Agency for International Development (USAID). https://reliefweb.int/attachments/6990395a-ac4d-39b0-839a-a562255d61e9/West_Africa_CRP_Final.pdf

Venegas, S. A., Mysak, L. A., & Straub, D. N. (1996). Evidence for interannual and interdecadal climate variability in the South Atlantic. *Geophysical Research Letters*, *23*(19), 2673–2676. https://doi.org/10.1029/96GL02373

Venegas, S. A., Mysak, L. A., & Straub, D. N. (1997). Atmosphere–Ocean Coupled Variability in the South Atlantic. *Journal of Climate*, *10*(11), 2904–2920. https://doi.org/10.1175/1520-0442(1997)010<2904:AOCVIT>2.0.CO;2

Volodin, E. M., Mortikov, E. V., Kostrykin, S. V., Galin, V. Ya., Lykossov, V. N., Gritsun, A. S., Diansky, N. A., Gusev, A. V., & Iakovlev, N. G. (2017). Simulation of the present-day climate with the climate model INMCM5. *Climate Dynamics*, *49*(11–12), 3715–3734. https://doi.org/10.1007/s00382-017-3539-7

Volodin, E. M., Mortikov, E. V., Kostrykin, S. V., Galin, V. Ya., Lykossov, V. N., Gritsun, A. S., Diansky, N. A., Gusev, A. V., Iakovlev, N. G., Shestakova, A. A., & Emelina, S. V. (2018). Simulation of the modern climate using the INM-CM48 climate model. *Russian Journal of Numerical Analysis and Mathematical Modelling*, *33*(6), 367–374. https://doi.org/10.1515/rnam-2018-0032

Wainer, I., Prado, L. F., Khodri, M., & Otto-Bliesner, B. (2021). The South Atlantic subtropical dipole mode since the last deglaciation and changes in rainfall. *Climate Dynamics*, *56*(1), 109–122. https://doi.org/10.1007/s00382-020-05468-z

Wang, Y., Heywood, K. J., Stevens, D. P., & Damerell, G. M. (2022). Seasonal extrema of sea surface temperature in CMIP6 models. *Ocean Science*, *18*(3), 839–855.

Wani, S., Singh, P., Boomiraj, K., & Sahrawat, K. (2009). Climate change and sustainable rain-fed agriculture: Challenges and opportunities. *Agricultural Situation in India*, *66*(5), 221–239.

Waskom, M. (2021). seaborn: Statistical data visualization. *Journal of Open Source Software*, *6*(60), 3021. https://doi.org/10.21105/joss.03021

Weber, T., Cabos, W., Sein, D. V., & Jacob, D. (2023). Benefits of simulating precipitation characteristics over Africa with a regionally-coupled atmosphere–ocean model. *Climate Dynamics*, *60*(3), 1079–1102. https://doi.org/10.1007/s00382-022-06329-7

Wiederhecker, H. C., Pinto, A. C. S., & Colli, G. R. (2002). Reproductive Ecology of Tropidurus torquatus (Squamata: Tropiduridae) in the Highly Seasonal Cerrado Biome of Central Brazil. *Journal of Herpetology*, *36*(1), 82–91. https://doi.org/10.1670/0022-1511(2002)036[0082:REOTTS]2.0.CO;2

Williams, C. J. R., Kniveton, D. R., & Layberry, R. (2008). Influence of South Atlantic Sea Surface Temperatures on Rainfall Variability and Extremes over Southern Africa. *Journal of Climate*, *21*(24), 6498–6520. https://doi.org/10.1175/2008JCLI2234.1

Woodruff, S. D., Diaz, H. F., Worley, S. J., Reynolds, R. W., & Lubker, S. J. (2005). Early ship observational data and ICOADS. *Climatic Change*, *73*(1–2), 169–194.

Woodruff, S. D., Slutz, R. J., Jenne, R. L., & Steurer, P. M. (1987). A comprehensive ocean-atmosphere data set. *Bulletin of the American Meteorological Society*, *68*(10), 1239–1250.

Wu, T., Lu, Y., Fang, Y., Xin, X., Li, L., Li, W., Jie, W., Zhang, J., Liu, Y., Zhang, L., Zhang, F., Zhang, Y., Wu, F., Li, J., Chu, M., Wang, Z., Shi, X., Liu, X., Wei, M., … Liu, X. (2019). The Beijing Climate Center Climate System Model (BCC-CSM): The main progress from CMIP5 to CMIP6. *Geoscientific Model Development*, *12*(4), 1573–1600. https://doi.org/10.5194/gmd-12-1573-2019

Wu, T., Zhang, F., Zhang, J., Jie, W., Zhang, Y., Wu, F., Li, L., Yan, J., Liu, X., Lu, X., Tan, H., Zhang, L., Wang, J., & Hu, A. (2020). Beijing Climate Center Earth System Model version 1 (BCC-ESM1): Model description and evaluation of aerosol simulations. *Geoscientific Model Development*, *13*(3), 977–1005. https://doi.org/10.5194/gmd-13-977-2020

Wu, Z., Huang, N. E., Long, S. R., & Peng, C.-K. (2007). On the trend, detrending, and variability of nonlinear and nonstationary time series. *Proceedings of the National Academy of Sciences*, *104*(38), 14889–14894. https://doi.org/10.1073/pnas.0701020104

Xie, S.-P., & Carton, J. A. (2004). Tropical Atlantic variability: Patterns, mechanisms, and impacts. *Earth's Climate: The Ocean-Atmosphere Interaction, Geophys. Monogr*, *147*, 121–142.

Yang, X., & Huang, P. (2023). Improvements in the relationship between tropical precipitation and sea surface temperature from CMIP5 to CMIP6. *Climate Dynamics*, *60*(11–12), 3319–3337.

Yang, X., Zhou, B., Xu, Y., & Han, Z. (2021). CMIP6 Evaluation and Projection of Temperature and Precipitation over China. *Advances in Atmospheric Sciences*, *38*(5), 817–830. https://doi.org/10.1007/s00376-021-0351-4

Yukimoto, S., Kawai, H., Koshiro, T., Oshima, N., Yoshida, K., Urakawa, S., Tsujino, H., Deushi, M., Tanaka, T., Hosaka, M., Yabu, S., Yoshimura, H., Shindo, E., Mizuta, R., Obata, A., Adachi, Y., & Ishii, M. (2019). The Meteorological Research Institute Earth System Model Version 2.0, MRI-ESM2.0: Description and Basic Evaluation of the Physical Component. *Journal of the Meteorological Society of Japan. Ser. II*, *97*(5), 931–965. https://doi.org/10.2151/jmsj.2019-051

Zebiak, S. E. (1993). Air–sea interaction in the equatorial Atlantic region. *Journal of Climate*, *6*(8), 1567–1586.

Ziehn, T., Chamberlain, M. A., Law, R. M., Lenton, A., Bodman, R. W., Dix, M., Stevens, L., Wang, Y.-P., & Srbinovsky, J. (2020). The Australian Earth System Model: ACCESS-ESM1.5. *Journal of Southern Hemisphere Earth Systems Science*, *70*(1), 193–214. https://doi.org/10.1071/ES19035

Appendix

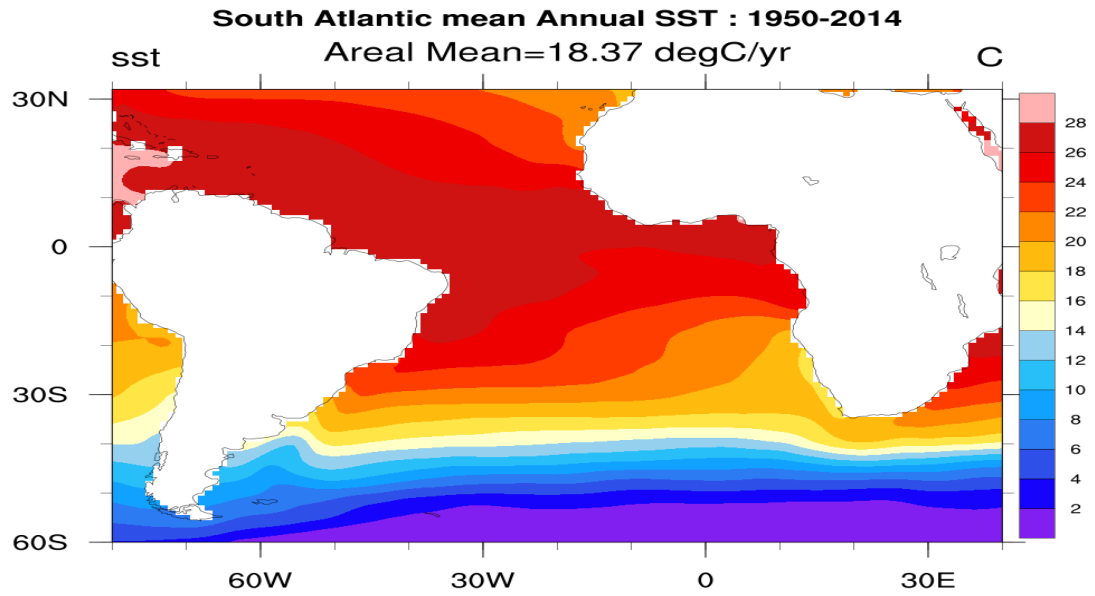

Figure A1: Mean Sea Surface Temperature (SST) in the South Atlantic for the historical period under consideration (1950 – 2014). Map is generated from global HadISST data.

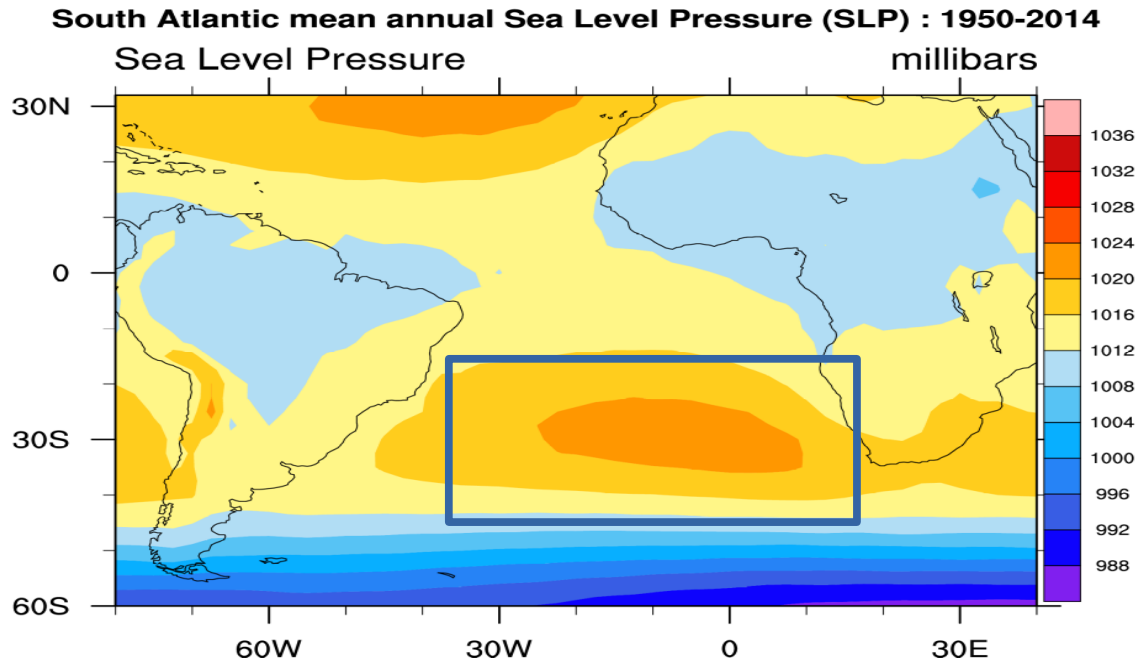

Figure A2: Mean Sea Level Pressure (SLP) in the South Atlantic region for the period of 1950 – 2014. The mean position of the St. Helena Anticyclone is indicated (Box).

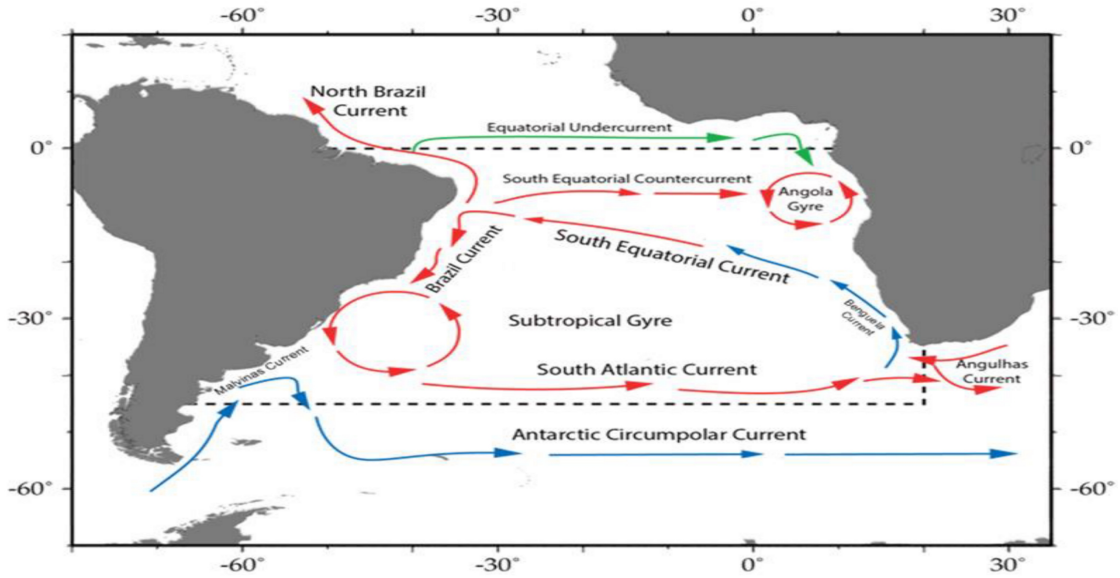

Figure A3: Schematic of major current systems in the South Atlantic region. Red arrows indicate generally warmer water currents; blue arrows indicate generally cooler water currents. (source: Muller-Karger et al., 2017)

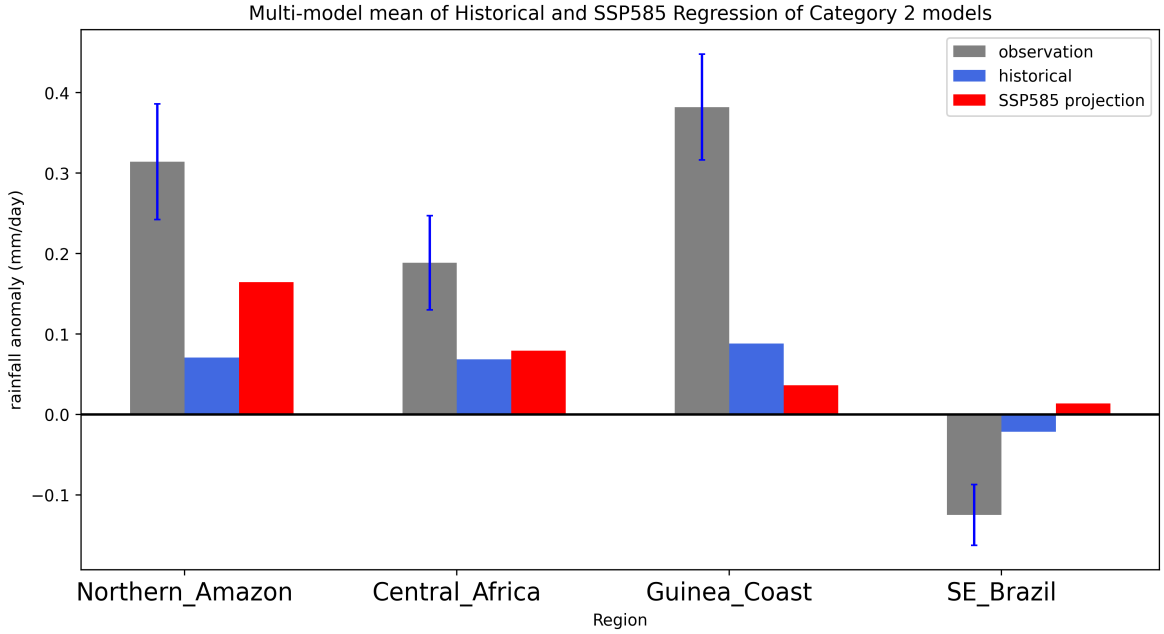

Figure A4: Ensemble mean of Category 2 models in each region. Standard error for observations are indicated.

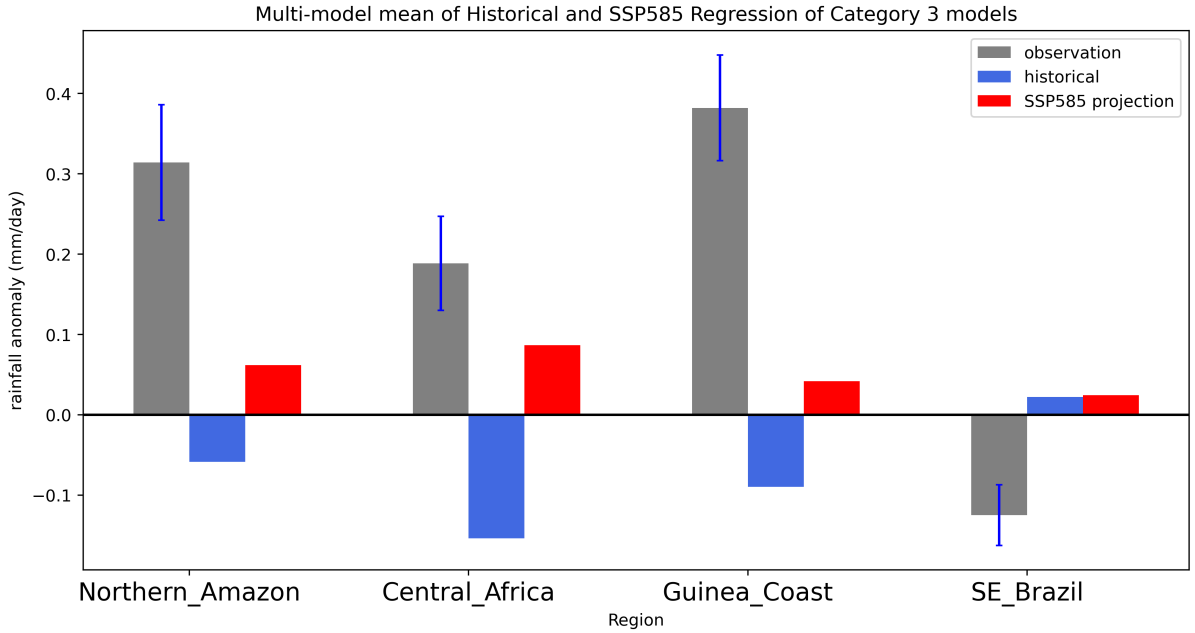

Figure A5: Ensemble mean of Category 3 models in each region. Standard error for observations are indicated.

Table A6: Models Categorized according to performance in each region

CATEGORY 1				
	Northern_Amazon	**Central_Africa**	**Guinea_Coast**	**SE_Brazil**
1	MRI-ESM2-0	E3SM-1-1	FIO-ESM-2-0	ACCESS-CM2
2	CMCC-CM2-SR5	CMCC-CM2-HR4	CMCC-ESM2	GFDL-ESM4
3	IPSL-CM6A-LR	E3SM-1-1-ECA	NorESM2-LM	ACCESS-ESM1-5
4	CanESM5	BCC-CSM2-MR	CMCC-CM2-SR5	
5	CMCC-ESM2	ACCESS-CM2	ACCESS-ESM1-5	
6	MPI-ESM1-2-HR	E3SM-1-0	SAM0-UNICON	
7	NorESM2-MM	EC-Earth3-AerChem	NorESM2-MM	
8	INM-CM5-0	CESM2		
9	NorCPM1	INM-CM4-8		
10	FIO-ESM-2-0	FGOALS-g3		
11	EC-Earth3-CC	MIROC6		
12	ACCESS-ESM1-5	IITM-ESM		

13	EC-Earth3	INM-CM5-0
14	MIROC6	MPI-ESM1-2-HR
15	GISS-E2-1-H	KACE-1-0-G
16		EC-Earth3
17		FIO-ESM-2-0
18		CMCC-CM2-SR5
19		EC-Earth3-CC
20		CMCC-ESM2
21		SAM0-UNICON
22		ACCESS-ESM1-5
23		NorESM2-MM

CATEGORY 2

	Northern_Amazon	**Central_Africa**	**Guinea_Coast**	**SE_Brazil**
1	SAM0-UNICON	MPI-ESM-1-2-HAM	E3SM-1-1-ECA	MESM3
2	FGOALS-g3	CESM2-WACCM	EC-Earth3-CC	FIO-ESM-2-0
3	CESM2-WACCM	CAS-ESM2-0	MCM-UA-1-0	CMCC-ESM2
4	KACE-1-0-G	MRI-ESM2-0	BCC-CSM2-MR	CESM
5	TaiESM1	MCM-UA-1-0	E3SM-1-1	EC-Earth3-AerChem
6	GISS-E2-1-G-CC	NESM3	CAS-ESM2-0	EC-Earth3-CC
7	CESM2	IPSL-CM6A-LR	MPI-ESM1-2-HR	MRI-ESM2-0
8	GFDL-ESM4	FGOALS-f3-L	CMCC-CM2-HR4	CMCC-CM2-SR5
9	AWI-ESM-1-1-LR	NorCPM1	NESM3	MPI-ESM-1-2-HAM
10	EC-Earth3-AerChem	MPI-ESM1-2-LR	CESM2	NorESM2-MM
11	MPI-ESM-1-2-HAM	AWI-CM-1-1-MR	MIROC6	AWI-CM-1-1-MR
12	BCC-CSM2-MR	BCC-ESM1	CESM2-WACCM	CAMS-CSM1-0
13	CMCC-CM2-HR4	NorESM2-LM	MPI-ESM1-2-LR	INM-CM5-0
14	BCC-ESM1	TaiESM1	AWI-CM-1-1-MR	BCC-CSM2-MR
15	CAMS-CSM1-0	CAMS-CSM1-0	EC-Earth3	FGOALS-g3
16	INM-CM4-8		KACE-1-0-G	CESM2-WACCM

17	NESM3		E3SM-1-0	E3SM-1-0
18	ACCESS-CM2		CAMS-CSM1-0	MIROC6
19				NorESM2-LM
20				MPI-ESM1-2-LR
	CATEGORY 3			
	Northern_Amazon	**Central_Africa**	**Guinea_Coast**	**SE_Brazil**
1	GISS-E2-1-G	GFDL-ESM4	TaiESM1	CanESM5
2	E3SM-1-1	AWI-ESM-1-1-LR	INM-CM4-8	CMCC-CM2-HR4
3	E3SM-1-0	GISS-E2-1-G	MPI-ESM-1-2-HAM	AWI-ESM-1-1-LR
4	MCM-UA-1-0	GISS-E2-1-H	MRI-ESM2-0	E3SM-1-1-ECA
5	IITM-ESM	GISS-E2-1-G-CC	BCC-ESM1	INM-CM4-8
6	E3SM-1-1-ECA	CanESM5	GFDL-ESM4	MPI-ESM1-2-HR
7	AWI-CM-1-1-MR		GFOALS-g3	EC-Earth3
8	FGOALS-f3-L		IPSL-CM6A-LR	CAS-ESM2-0
9	MPI-ESM1-2-LR		CanESM5	BCC-ESM1
10	NorESM2-LM		INM-CM5-0	SAM0-UNICON
11	CAS-ESM2-0		GISS-E2-1-G-CC	IPSL-CM6A-LR
12			EC-Earth3_AerChem	KACE-1-0-G
13			GISS-E2-1-H	E3SM-1-1-ECA
14			FGOALS-f3-L	FGOALS-f3-L
15			ACCESS-CM2	IITM-ESM
16			IITM-ESM	GISS-E2-1-H
17			NorCPM1	NorCPM1
18			GISS-E2-1-G	TaiESM1
19			AWI-ESM-1-1-LR	GISS-E2-1-G
20				MCM-UA-1-0
21				GISS-E2-1-G-CC

Data availability

Observations datasets for SST and rainfall were obtained from the UK Met Office Hadley Centre website (https://www.metoffice.gov.uk/hadobs/hadisst/data/download.html) and the Deutscher Wetterdienst (DWD, National Meteorological Service of Germany) website (https://opendata.dwd.de/climate_environment/GPCC/html/fulldata-monthly_v2022_doi_download.html), respectively while CMIP6 model outputs were obtained from the German Climate Computing Centre (DKRZ) supercomputer database (https://esgf-data.dkrz.de/projects/cmip6-dkrz/).

All data files used in this work are freely available via their respective websites.